Article

Lysosomal "TRAP": a neotype modality for clearance of viruses and variants

Chengliang Lyu [1,2,3,13], Zhanlong He[4,13], Xiaoming Hu[1,2,5,13], Shuang Wang [1,2,5], Meng Qin[6], Li Zhu [7], Yanyan Li[4], Fengmei Yang[4], Zhouguang Jiao[1], Xiao Zhang[1,2,5], Guihong Lu [1], Erqiang Wang[8], Yaling Hu[8], Yu Zhai[8], Youchun Wang [9], Weijin Huang [9], Dongshu Wang[7], Yimin Cui[10,11], Xiaocong Pang[10,11], Xiangzheng Liu[12], Hidehiro Kamiya[3], Guanghui Ma [1,2,5] ✉ & Wei Wei [1,2,5] ✉

The binding of viruses to host-entry factor receptors is an essential step for viral infection. Many studies have shown that macrophages can internalize viruses and degrade them in lysosomes for clearance in vivo. Inspired by these natural behaviors and using SARS-CoV-2 as a testbed, we harvest lysosomes from activated macrophages and anchor the protein-receptor ACE2 as bait, thus constructing a lysosomal "TRAP" (lysoTRAP) that selectively captures, internalizes, and eventually degrades SARS-CoV-2. Through experiments with cells, female mice, female hamsters, and human lung organoids, we demonstrate that lysoTRAP effectively clears SARS-CoV-2. Importantly, unlike therapeutic agents targeting SARS-CoV-2 spike protein, lysoTRAP remains effective against nine pseudotyped variants and the authentic Omicron variant, demonstrating its resistance to SARS-CoV-2 mutations. In addition to the protein-receptor ACE2, we also extend lysoTRAP with the saccharide-receptor sialic acid and verify its excellent antiviral effect against H1N1, highlighting the flexibility of our "TRAP" platform in fighting against various viruses.

Viral infections pose a serious threat to human health and safety. For instance, it is estimated that there were up to 575,400 deaths worldwide during the influenza pandemic in 2009; the ongoing COVID-19 pandemic caused by severe acute respiratory syndrome coronavirus 2 (SARS-CoV-2) also has resulted in a staggering over 7.05 million deaths as the data from the World Health Organization (WHO) [1-3]. For a typical SARS-CoV-2 infection, the receptor-binding domain (RBD) of the spike (S) protein specifically binds to the host protein-receptor ACE2, which is known to be essential for the entry of SARS-CoV-2 into cells[4-6]. Multiple studies have explored the development of medical agents to prevent this binding, such as antibodies against S protein and the small-molecule inhibitors with high affinity to the S protein[7-10].

[1]State Key Laboratory of Biochemical Engineering, Institute of Process Engineering, Chinese Academy of Sciences, Beijing 100190, China. [2]Key Laboratory of Biopharmaceutical Preparation and Delivery, Chinese Academy of Sciences, Beijing 100190, China. [3]Graduate School of Bio-Applications and Systems Engineering, Tokyo University of Agriculture and Technology, Tokyo 184-8588, Japan. [4]Institute of Medical Biology, Peking Union Medical College & Chinese Academy of Medical Sciences, Yunnan Key Laboratory of Vaccine Research Development on Severe Infectious Disease, Kunming 650118, China. [5]School of Chemical Engineering, University of Chinese Academy of Sciences, Beijing 100049, China. [6]Beijing Advanced Innovation Center for Soft Matter Science and Engineering, College of Life Science and Technology, Beijing University of Chemical Technology, Beijing 100029, China. [7]State Key Laboratory of Pathogen and Biosecurity, Beijing Institute of Biotechnology, Beijing 100071, China. [8]Sinovac Life Sciences Co., Ltd., Beijing 100085, China. [9]Division of HIV/AIDS and Sex-Transmitted Virus Vaccines, Institute for Biological Product Control, National Institutes for Food and Drug Control (NIFDC) and WHO Collaborating Center for Standardization and Evaluation of Biologicals, Beijing 102629, China. [10]Department of Pharmacy, Peking University First Hospital, Beijing 100034, China. [11]Institute of Clinical Pharmacology, Peking University, Beijing 100191, China. [12]Department of thoracic surgery, Peking University First Hospital, Beijing 100034, China. [13]These authors contributed equally: Chengliang Lyu, Zhanlong He, Xiaoming Hu. ✉e-mail: ghma@ipe.ac.cn; weiwei@ipe.ac.cn

However, the effectiveness of these agents (and virtually all vaccines) relies on their specificity to the S protein and such strategies can be rendered ineffective by S protein mutations[11–14], which are now known to occur frequently and pose a continuous threat to public health[15,16].

Macrophage-mediated clearance is now well known as a defense against most viral infections[17,18]. Taking SARS-CoV-2 for example, basic and clinical studies have demonstrated that macrophages in the lung can internalize SARS-CoV-2 virions, which are subsequently degraded in lysosomes[19–22]. Inspired by these natural behaviors of viral binding and clearance, we envisioned a therapeutic approach for selectively "internalizing" and "eliminating" SARS-CoV-2 inside lysosomes that are decorated with the ACE2 on the exterior as "bait". That is, we aimed to mimic the function of macrophages for the clearance of SARS-CoV-2 by capturing, internalizing, and degrading SARS-CoV-2, using a material that is much easier to store, handle, and therapeutically deliver than macrophages.

In this work, we initially harvest lysosomes from activated macrophages and anchor the ACE2 receptor on the exterior, thus constructing a lysosomal "TRAP" (lysoTRAP)[23,24]. The resulting "lysoTRAP" shows good stability, and retains the desired functions, including specifically capturing and internalizing SARS-CoV-2, and efficiently degrading the internalized virions, leading to in vitro potent clearance of pseudotyped SARS-CoV-2 (wild-type) and additional nine different variants. Furthermore, in vivo administration of lysoTRAP via pulmonary inhalation leads to rapid accumulation of lysoTRAP in the lung without any visible abnormalities, and the potent clearance of pseudotyped and authentic SARS-CoV-2 is verified in mouse and hamster infection models. Finally, we construct a human lysoTRAP (h-lysoTRAP), reveal authentic SARS-CoV-2 degradation mechanism and demonstrate its superior clearance activity against SARS-CoV-2 and its extraordinary inhibition of viral infection over that of RBD antibody and inhibitor (EIDD2801: nucleoside analogue) in human lung organoids. To highlight the flexibility of our "lysoTRAP", we also replace the protein-receptor ACE2 with the saccharide-receptor sialic acid (SA), which enables efficient clearance of two influenza A (H1N1) variants and potent inhibition of their infection. Overall, our study provides a proof-of-concept demonstration for the potential anti-virus strategy by using "TRAP" platform as a neotype and general virus clearance agent.

Results

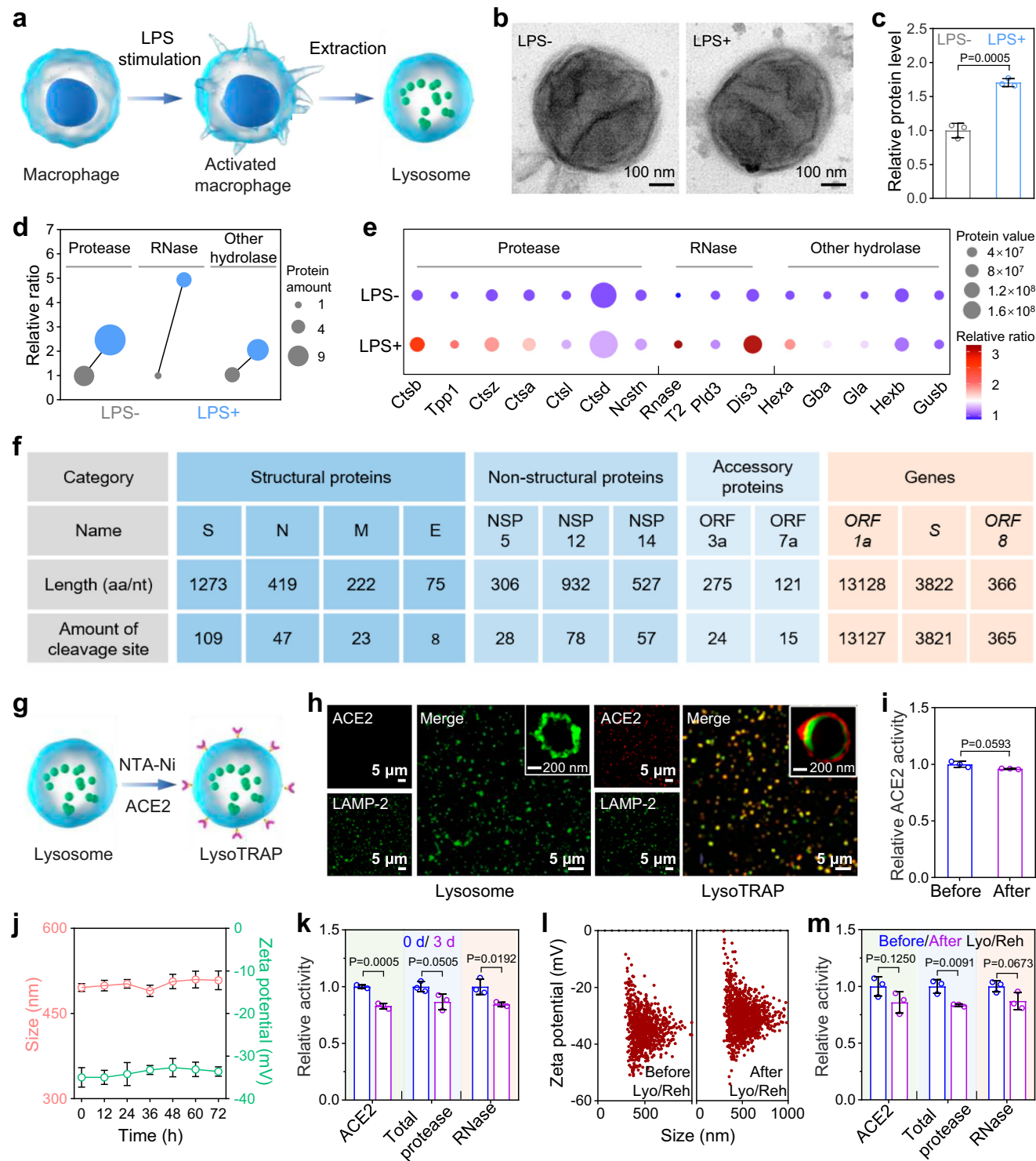### Construction and characterizations of lysoTRAP for SARS-CoV-2

Prior to construct the lysoTRAP system, we optimized lysosome production step (Fig. 1a). As activated macrophages are known for their pathogen clearance activity, therefore we reasoned that lysosomes from activated macrophages should have enhanced virion degradation activity. To this end, mouse-derived primary macrophages were activated with lipopolysaccharide (LPS) treatment (Fig. S1). Upon physical disruption and differential centrifugation, lysosomes were harvested with good reproducibility (Fig. S2a−c) and characterized in detail. Transmission electron microscopy (TEM) images revealed no obvious morphological difference between lysosomes isolated from LPS stimulated macrophages (LPS+) and untreated macrophages (LPS-) (Fig. 1b). Nevertheless, LPS+ group showed an elevated protein content, with approximately 1.6 times over that of LPS- group (Fig. 1c). Upon liquid chromatography-mass spectrometry (LC-MS) proteomic analysis, we further found that the levels of most proteases and ribonucleases (RNase) were substantially enriched in the LPS+ group (Fig. 1d, e), justifying the choice for activated macrophage derived lysosomes as the source for lysoTRAP with a superior SARS-CoV-2 degradation activity. According to the enzymatic mechanisms of proteases and RNases[25,26], we analyzed the potential degradation profiles of viral proteins and genes (wild-type) (Fig. 1f). For example, both non-structural protein 5 (NSP5) and *open reading frame 1a* (*ORF1a*) showed plentiful cleavage sites for degradation with 28 and 13271 enzymatic cleavage sites, respectively.

Following lysosome optimization, we started our construction of lysoTRAP against SARS-CoV-2. Briefly, amphiphilic 1,2-distearoyl-sn-glycero-3-phosphoethanolamine-N-[amino(polyethylene glycol)-2000](nitrotriacetic acid-nickel) (DSPE-PEG-NTA-Ni) was inserted into the membrane of the lysosomes (Fig. 1g). By exploiting the strong chelation between the NTA-Ni group and the polyhistidine (His) tag of ACE2 (recombinant protein with extracellular domain of human ACE2 (Met1-Ser740) and a His tag at the C-terminus), the known SARS-CoV-2 entry-point protein was anchored to the lysosome exterior to form the lysoTRAP with good reproducibility (Fig. S2d). This anchorage had no effect on the morphology of lysosomes and was verified with the co-localization of ACE2 and lysosomal associated membrane protein-2 (LAMP-2) signals by using confocal laser scanning microscopy (CLSM) and stimulated emission depletion microscopy (STED) images (Figs. 1h, S3a, and S3b), as well as slightly increased particle size and zeta potential (Fig. S3c). Furthermore, quantification of the anchored ACE2 on the lysosomes was performed by enzyme-linked immunosorbent assay (ELISA) measurement, and the calculation revealed a loading content upto 5600 ACE2 molecules per lysosome (Fig. S3d). Additionally, we validated that over 90% of ACE2 enzymatic activity, protease enzymatic activity (including activities of total proteases, Cathepsin L, and Cathepsin B), RNase enzymatic activities, and acid environment were retained after the anchorage process (Figs. 1i and S3e-h), thus paving the way for the efficient binding and degradation of SARS-CoV-2.

We next conducted multiple experiments to verify the lysoTRAP stability. During 72 hours (h) incubation in PBS solution at 37 °C, lysoTRAP showed slight change in the particle size or zeta potential (Fig. 1j), and almost no ACE2 detachment or protease and RNase leakage was found in the external medium (Fig. S3i), together indicating that the stable structure of lysoTRAP restricted the release of ACE2 and enzymes. Consequently, over 80% of the ACE2, protease and RNase enzymatic activities in lysoTRAP were retained after 72 h incubation at 37 °C (Fig. 1k), suggesting the stable biological activity for in vivo use (Fig. S4). Given the profound impact of long-term storage for biomedical applications, we also assessed the stability of lyophilized lysoTRAP. Even after a six-month preservation at 4 °C, rehydrated lysoTRAP showed almost no significant changes in multiple critical indicators, such as particle size, zeta potential, acid environment, the activities of enzymes (ACE2, total proteases, Cathepsin L, Cathepsin B, and RNases) (Figs. 1l, m, and S5). These results thus indicated that lysoTRAP could be lyophilized and long-term stored without functional degradation.

Evaluations of the performance of lysoTRAP in capturing, internalizing, and degrading pseudotyped SARS-CoV-2 virions

With lysoTRAP in hand, we next evaluated the in vitro performance of lysoTRAP in capturing, internalizing, and degrading SARS-CoV-2 (Fig. 2a). Herein, we utilized pseudotyped SARS-CoV-2 virions (wild-type), which were prepared as lentiviral vectors by using a pseudotyped virus packaging system of human immunodeficiency virus (HIV) with expressing S protein at the capsid membrane surface along with containing green fluorescent protein (GFP) and luciferase (Luc) RNA (*GFP* and *Luc*) internal reporter genes. Firstly, specific virion capture activity of lysoTRAP was evaluated using a quartz crystal microbalance (QCM) detection (Fig. 2b). Briefly, the lysosomal materials were evenly affixed onto the chip surface and then exposed to the flow of pseudotyped virions. Compared with naked lysosome group, the lysoTRAP group showed a substantially decreased △ frequency, indicating a strong interaction between the lysoTRAP and the pseudotyped virions. Above frequency variation was substantially compromised when pretreating with ACE2 antibody (anti-ACE2) or using pseudotyped control virions (without SARS-CoV-2 S protein) (Figs. S6−7). Those results demonstrated the specificity binding of ACE2 protein on lysoTRAP to S protein on pseudotyped SARS-CoV-2 virions for capturing the virions.

Category	Structural proteins				Non-structural proteins			Accessory proteins		Genes		
Name	S	N	M	E	NSP 5	NSP 12	NSP 14	ORF 3a	ORF 7a	*ORF 1a*	*S*	*ORF 8*
Length (aa/nt)	1273	419	222	75	306	932	527	275	121	13128	3822	366
Amount of cleavage site	109	47	23	8	28	78	57	24	15	13127	3821	365

To evaluate the performance of lysoTRAP internalizing pseudotyped SARS-CoV-2 virions, we herein used three imaging methods. Real-time CLSM imaging revealed a dynamic internalization process, which included 4-bora-3a,4a-diaza-s-indacene (BODIPY) -labeled pseudotyped virions 1) initially adhering to the Cyanine 5 (Cy5) -labeled lysoTRAP surface, 2) crossing the lysoTRAP membrane, and 3) finally being restricted inside the lysoTRAP (Fig. 2c). For higher resolution, we also performed STED and TEM, which clearly showed BODIPY-labeled pseudotyped virions restricted inside the lysoTRAP (Fig. 2d). To reveal internalization mechanism, we further conducted fluorescence resonance energy transfer (FRET) analysis via pro-

labeling lysoTRAP (lysosomes) with Cyanine 7 (Cy7) and pseudotyped SARS-CoV-2 virions with Cyanine 5.5 (Cy5.5) (Fig. S8a). After 1 h incubation, we found a typical FRET performance with a remarkably increased Cy7 fluorescence intensity in the lysoTRAP group rather than in the lysosome group (Fig. S8b). This result indicated that lysoTRAP internalized pseudotyped SARS-CoV-2 virions via a potential membrane fusion, which might rely on the cleavage of S protein by the Furin on the lysoTRAP (Fig. S9).

Given that the pseudotyped virions comprised inner structural protein P55, inner capsid protein P24 and two reporters (*GFP* and *Luc*), we further utilized ELISA, western blotting (WB), quantitative

Fig. 1 | Construction and characterizations of lysoTRAP. a Schematic for lysosome purification. Primary macrophages were stimulated with lipopolysaccharides (LPS) to generate activated macrophages, which was followed by the isolation of lysosomes via physical disruption and differential centrifugation. **b** Transmission electron microscopy (TEM) images of the lysosomes isolated from macrophages stimulated with LPS (LPS+) or without LPS (LPS-). **c** Protein levels of the lysosomes (same number) isolated from macrophages stimulated with or without LPS, showing increased protein levels following LPS stimulation. **d** Proteomic analysis of hydrolase levels in the lysosomes from macrophages stimulated with or without LPS via liquid chromatography–mass spectrometry (LC-MS). Relative ratio was normalized according to the LPS- group. **e** Levels of representative hydrolases in lysosomes based on proteomic data. Protein value was derived from LC-MS data and the relative ratio was normalized according to the LPS- group. **f** Theoretical analysis of enzymatic cleavage sites of SARS-CoV-2 (wild-type) representative proteins and genes according to the enzymatic mechanisms of proteases and RNases inside lysosomes. **g** Schematic for construction of lysoTRAP. An amphiphilic compound-DSPE-PEG-NTA-Ni was inserted into the membrane of the lysosomes, followed by anchoring ACE2-His tag fusion protein through NTA-Ni/His affinity, thus creating our "lysoTRAP". **h** Confocal laser scanning microscopy (CLSM) images and inserted stimulated emission depletion microscopy (STED) images of naked lysosomes and lysoTRAP, showing successful anchorage of ACE2 to the lysoTRAP membrane. **i** Enzymatic activities of ACE2 before and after ACE2 anchorage to lysosome. **j** Physical stability of lysoTRAP over a 72-hour incubation in phosphate buffered saline (PBS) at 37 °C, detected by the size and zeta potential. **k** Biological stability of lysoTRAP over a 72-hour incubation in PBS at 37 °C, detected by the enzymatic activities of ACE2, total proteases and RNases. **l** Physical stability of lysoTRAP before and after lyophilization and rehydration (Lyo/Reh). **m** Biological stability of ACE2, total protease and RNase in the lysoTRAP before and after Lyo/Reh. The data in **c, i, j, k,** and **m** represent the mean ± S.D. (n = 3 biologically independent experiments). Statistical significance was calculated using two-tailed unpaired t-test in **c, i, k,** and **m**. Source data were provided in the Source data file.

polymerase chain reaction (q-PCR) and RNA electrophoresis to evaluate the degradation performance of lysoTRAP with these indicators. Monitoring over a time series, a gradual decrease in viral proteins and genes was observed in the lysoTRAP group with almost complete signal loss after 24 h, while slightly decreased signals were observed in the PBS group (Figs. 2e, f, and S10). Once the acidification inhibitor or the hydrolase inhibitors (including protease inhibitors and RNase inhibitor) were applied, the degradation of virions was largely compromised (Fig. S11). This result suggested that the complete degradation of pseudotyped virions should be attributed to proteases, RNases, and acid environment inside lysoTRAP rather than natural degradation. Moreover, almost no degradation signals of viral protein or RNA were detected after incubating lysoTRAP with the above-mentioned control virions, which could be attributed to the fact that the control virions failed to enter the lysoTRAP due to the lack of active S protein (Fig. S12). Note that trapping capacity could reach upto 13.3 pseudotyped virions per lysoTRAP, and yet these pseudotyped virions could still be fully degraded even upon such a high appetite (Fig. S13a).

Efficient inhibition of pseudotyped SARS-CoV-2 virion infection by lysoTRAP

Above results encouraged us to conduct a series of cellular assays (using ACE2-overexpressed (ACE2-OE) HEK293T cells) for examining the capacity of lysoTRAP to inhibit pseudotyped SARS-CoV-2 virion (wild-type) infection. The tested samples included naked lysosomes, free ACE2 protein, and lysoTRAP. The *GFP* reporter of pseudotyped SARS-CoV-2 virions facilitated us to carry out a standard host cell infection assay involving CLSM and flow cytometry analysis. CLSM images showed that as expected the pseudotyped virions could infect ACE2-OE HEK293T cells when treated with PBS or naked lysosomes (Fig. 2g). On the contrary, lysoTRAP-treated cells showed a significantly reduced GFP signal, and virtually no GFP signal was detected within the cells. Once the free ACE2 protein was applied, pseudotyped virion infection to the cells was intermediated. Similar results were also obtained from the flow cytometry analysis, where virion infection was remarkably suppressed, with an infected cell rate of less than 2% in the lysoTRAP group. Inhibition of lysoTRAP was also observed with a dose-dependent pattern, and the calculated half maximal inhibitory concentration (IC50) of lysoTRAP was far below that of the free ACE2 protein, with over 20-fold decrease (Fig. S13b).

We also conducted a standard virus titration method to assess the impact of these samples. Although both free ACE2 and lysoTRAP reduced the viral titers, the reduction from lysoTRAP significantly outperformed free ACE2 by two orders of magnitude (Fig. S13c). These results further indicated that the unique trapping property of lysoTRAP, rather than its ACE2 simple binding behavior, was responsible for the superior inhibitory activity against SARS-CoV-2 virions. Given that SARS-CoV-2 mutations can restrict or abrogate therapeutic and prophylactic activities, we next assessed whether the inhibitory activity of lysoTRAP on the virions was resistant to S mutations. Nine different pseudotyped variants with S protein mutations (including the D614G strain, three variants of interest (VOI) and five variants of concern (VOC)) were prepared by using a pseudotyped virus packaging system of vesicular stomatitis virus (VSV) and utilized in the virus infection assay with the same cellular model using a *Luc* reporter system (Fig. 2h). In this system, we excitingly found none of these S protein mutations disrupted the capacity of lysoTRAP to inhibit viral infection due to the ACE2-mediated trapping, thus ignoring the major concern of frequent mutations that arose in the ongoing COVID-19 pandemic.

In vivo biodistribution and trapping SARS-CoV-2 performance of lysoTRAP administered by pulmonary inhalation

The excellent anti-infectivity performance of lysoTRAP from our in vitro assays encouraged us to assess in vivo performance, which we initiated by comparatively testing the in vivo biodistribution via two administration routes (Fig. S14). Briefly, Cy7-labeled lysoTRAP was administered via intravenous (*i.v.*) injection or pulmonary inhalation, and real-time in vivo fluorescence imaging was used to assess lysoTRAP biodistribution (Fig. 3a). Focusing on the lung area, while both administration routes resulted in strong lysoTRAP fluorescence signals peaking at 9 h of post-administration, pulmonary inhalation exhibited stronger intensity in the lung, with a 2.4 times area under the curve (AUC) higher than that of *i.v.* injection (Fig. 3b). Subsequently ex vivo imaging of the main organs at 9 h of post-administration and the corresponding fluorescence intensity analyses showed that the Cy7 signals in pulmonary inhalation group were evident in the lungs, but not in other organs (*e.g.*, liver or spleen) (Fig. 3c). Correspondingly, 73.9% of lysoTRAP remained in the lungs 9 h after pulmonary inhalation, which was almost eight times higher than the retention noticed after *i.v.* injection. Taken together, these results revealed that pulmonary inhalation was a more sensible administration route compared with the *i.v.* injection for an in vivo SARS-CoV-2 infection study.

Having demonstrated the rationality of pulmonary inhalation, we used scanned light-sheet microscopy for analyzing lysoTRAP distribution in the lung tissue with a high resolution. A shown in Fig. 3d, a large amount of lysoTRAP spread from the trachea and infiltrated deep into the lung tissue. Moreover, we investigated the biosafety of lysoTRAP in the aspects of endotoxin level, lung hematoxylin and eosin (H&E) staining, cytokine levels and lung respiratory function. As shown in the Fig. S15a, the endotoxin level per 1 mg lysoTRAP was detected as 0.17 EU, which was lower than the endotoxin limit (0.25 EU/mg, USP 36). Although the inhalation of lysoTRAP could induce slight and transient inflammation, it is reassuring to note that any such inflammation resolved within one week, even with further increases in dose and frequency (Figs. 3e-g and S15-18). Further taking the low
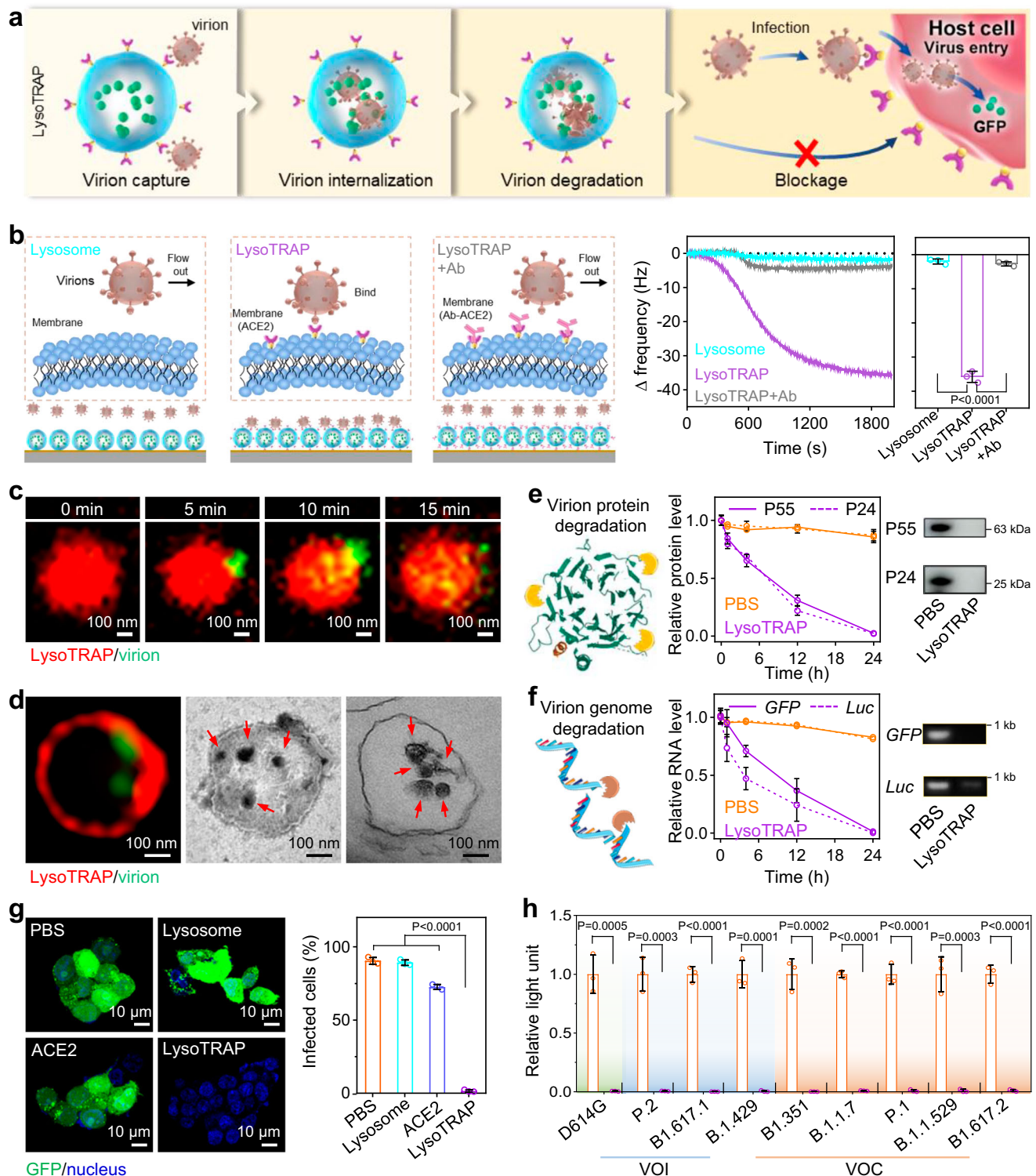
immunogenicity of lysoTRAP into consideration (Fig. S19), we thus envisioned that the pulmonary inhalation of this natural vesicle-based therapeutic had a wide therapeutic window, holding potential to be deployed for different courses of COVID-19.

Encouraged by the abovementioned results, we continued to investigate the in vivo performance of lysoTRAP. Briefly, 1×10^6 TU BODIPY-labeled pseudotyped virions (wild-type) were administrated into C57BL/6 mice via thoracic injection. 1 h later, Cyanine 5 (Cy5)-labeled samples (free ACE2, naked lysosomes, or lysoTRAP) were administrated via pulmonary inhalation (Fig. 3h). After 24 h, lung

tissues were collected for histological observation. Consistent with the in vitro data, almost no co-localization of naked lysosomes with pseudotyped virions along the white dotted line in the images was observed (Fig. 3i). In contrast, co-localization was evident upon lyso-TRAP or free ACE2 groups. Note that the co-localization area was much higher in the lysoTRAP group, again indicating a superior performance of lysoTRAP over that of free ACE2. Moreover, we assessed pseudo-typed virion degradation by WB and q-PCR. Both protein components (P55 and P24) and RNA component (*GFP*) were barely detectable at 48 h of post-inoculation (Figs. 3j and k), suggesting the efficient

Fig. 2 | Evaluations of programmed performance of lysoTRAP in capturing, internalizing, and degrading pseudotyped SARS-CoV-2 virions, causing efficient inhibition of viral infection. a Schematic for showing the designed SARS-CoV-2 clearance mechanism by lysoTRAP. **b** Schematic illustration for quartz crystal microbalance (QCM) experiment. Corresponding QCM curves and the change of the frequency of each group were displayed on the right panels. **c** CLSM images of Cy5-labeled lysoTRAP co-incubated with BODIPY-labeled pseudotyped virions, showing the process of pseudotyped virion internalization by lysoTRAP. **d** STED image showing a high magnification of Cy5-labeled lysoTRAP with internalized BODIPY-labeled pseudotyped virions after a 4-hour co-incubation. Corresponding TEM imaging and TEM section observation were displayed on the right panels. The internalized pseudotyped virions were indicated by red arrows in lysoTRAP. **e** Enzyme-linked immunosorbent assay (ELISA) measurement of viral protein levels (P55 and P24: structural proteins in the pseudotyped virions) after lysoTRAP or PBS incubation for indicated time points. Corresponding western blotting (WB) results of the 24-hour incubated sample were displayed on the right panel. **f** Quantitative polymerase chain reaction (q-PCR) analysis of viral RNA levels (*GFP* and *Luc*) after incubating with lysoTRAP or PBS for indicated time points. Corresponding agarose gel electrophoresis results of the 24-hour incubated sample were displayed on the right panel. **g** CLSM images of viral infection in ACE2-OE HEK293T cells and corresponding flow cytometry analysis. Both CLSM and flow cytometry analysis were assessed based on the GFP expression. In the infection assays, virions and lysoTRAP (PBS, lysosome or ACE2) were cultured with host cells at the same time. **h** Infection assays using additional pseudotyped virions carrying the S protein mutations (each with a *Luc* reporter to support quantification). The variants included the D614G strain, three variants of interest (VOI) and five variants of concern (VOC). The data in **b, e, f, g,** and **h** represent the mean ± S.D. (*n* = 3 biologically independent experiments). Statistical significance was calculated using a two-tailed one-way ANOVA with multiple comparison tests in **b** and **g,** and two-tailed unpaired *t*-test in **h.** Source data were provided in the Source data file.

degradation of pseudotyped virions after lysoTRAP treatment, even in a complex physiological environment.

In vivo clearance of SARS-CoV-2 by lysoTRAP

Having experimentally confirmed the trapping performance in vivo, we next examined the clearance capacity of lysoTRAP against pseudotyped virions for inhibiting viral infection in the human ACE2-expressing (hACE2) mouse model. Briefly, 1×10^6 TU pseudotyped virions (wild-type) were administrated into hACE2 C57BL/6 mice via thoracic injection (Fig. 4a). 1 h later, samples (free ACE2, naked lysosomes, or lysoTRAP) were administered via pulmonary inhalation. 2 d after viral inoculation, lung tissues were collected for histological observation of GFP signal upon infection. As expected, PBS and naked lysosome groups showed strong GFP signals throughout the lung tissue and corresponding histological slides (Fig. 4b, c). This was ameliorated in the ACE2 group, since the binding of ACE2 to pseudotyped virions slightly inhibited the infection. Owing to the fully verified trapping performance of capturing, internalizing, and degrading pseudotyped virions by lysoTRAP, this treatment resulted in little-to-no GFP signals observed in either the lung tissue or slide. Quantitively, compared with the PBS group, GFP intensity in lysoTRAP-treated mice was suppressed by less than 5%, implying that pseudotyped virions were very efficiently cleared by lysoTRAP in vivo. With the extensive concern about increased mutations of SARS-CoV-2, we further conducted pseudotyped virion infection analysis with the Omicron variant in the hACE2 mouse model and found undisturbed capacity of lysoTRAP in clearing virions and inhibiting viral infection (Fig. 4d, e), again showing the consistent performance of lysoTRAP confronted with unremitting and unpredictable mutations of SARS-CoV-2.

Above results encouraged us to further evaluate the clearance capacity of lysoTRAP against authentic SARS-CoV-2 in hamsters, which are being considered as a more credible COVID-19 model due to the similar viral infection processes and pathological features to human[27,28]. Briefly, hamsters were challenged with 2×10^4 50% tissue culture infective dose (TCID50) authentic SARS-CoV-2 via the intranasal route (Fig. 4f). Subsequently, the hamsters were randomized into two groups, which received pulmonary inhalation of either PBS or lysoTRAP (sourced from hamster macrophages and prepared with the same procedure aforementioned) at a dose of 5 mg particles per kg of body weight at 1 h, 1 d and 2 d of post-challenge. At 3 d, the lung tissues were collected for viral burden and histological analysis. Compared with PBS group, lysoTRAP group showed over 3 log reduction in viral genomic RNA copies of both wild-type SARS-CoV-2 and Omicron variant (Fig. 4g, k), indicating a drastic clearance of authentic SARS-CoV-2 virions in the lungs. Supporting this distinct viral burden, immunofluorescent staining of lung sections displayed strong signals of SARS-CoV-2 S1 protein in the PBS group rather than in the lysoTRAP group (Fig. 4h, l). Consequently, PBS group revealed typical signs of viral pneumonia, including expansion of alveolar septa, mononuclear cell

infiltrates, and consolidation, whereas almost no histopathological signs were detected in the lysoTRAP group (Fig. 4i, m), which was consistent with the results of inflammatory cytokine analysis in the lungs (Fig. 4j, n). Notably, negligible difference about lysoTRAP's clearing capacity was observed between the wild-type and Omicron variant, again confirming that the clearance capacity of lysoTRAP was undisturbed upon the mutations of SARS-CoV-2.

Construction of human lysoTRAP and the performance of trapping authentic SARS-CoV-2 in vitro

To support the clinical applicability, we continued to develop a human lysoTRAP (h-lysoTRAP) and evaluated its performance to authentic SARS-CoV-2 (Fig. 5a). For the h-lysoTRAP construction, human blood samples were incubated with Dynabeads to purify CD14 cells. Upon treatment with granulocyte-macrophage colony-stimulating factor (GM-CSF), these cells differentiated into macrophages and were further activated by LPS stimulation. Finally, purified human lysosomes (h-lysosome) were isolated from these macrophages and then anchored with ACE2 using the same procedure as described for producing lysoTRAP (mouse) to obtain h-lysoTRAP. As shown in Fig. 5b, h-lysoTRAP retained a typical vesicle morphology, with the diameter of approximately 500 nm. Further co-localization of ACE2 and LAMP-2 signals in the CLSM and STED images demonstrated successful ACE2 anchorage (Figs. 5c and S20a), which had very tiny effect on the enzymatic activities (total proteases, Cathepsin L, Cathepsin B, RNases, and ACE2) and acid environment of h-lysoTRAP (Figs. 5d and S20b-c).

The performance of the fabricated h-lysoTRAP with regard to trapping authentic SARS-CoV-2 was next characterized (Fig. 5e). As shown in Fig. 5f, h-lysoTRAP group showed a substantially decreased △ frequency signal compared to that of naked lysosome group, indicating successful capture of authentic SARS-CoV-2 (wild-type) by h-lysoTRAP. In term of internalization, TEM images provided visual evidences that virions were restricted inside h-lysoTRAP (Fig. 5g).

To investigate the degradation activity of proteases, we conducted proteomic analysis of h-lysoTRAP with trapped authentic SARS-CoV-2. Over time, a gradual decrease was observed in peptide fingerprints of SARS-CoV-2 proteins identified by LC-MS (Fig. 5h). Upon quantification of both amount and total intensity of the identified peptides, we found that protein degradation of lysoTRAP group mainly occurred within 6 h and almost ceased at 24 h. Focusing on the representative viral proteins at 24 h, compared with PBS group, viral outer membrane proteins (such as S and M) of lysoTRAP group showed a lower degradation proportion (Fig. 5i), as these proteins could avoid hydrolysis by remaining at the lysosome membrane after membrane fusion mediated internalization. On the contrary, viral inner proteins (such as NSP1, NSP2, NSP3, and NSP5) of lysoTRAP group were released into the lysosome interior during the internalization, leading to higher degradation proportion in these proteins. To gain a deeper insight into the residual SARS-CoV-2 peptides after
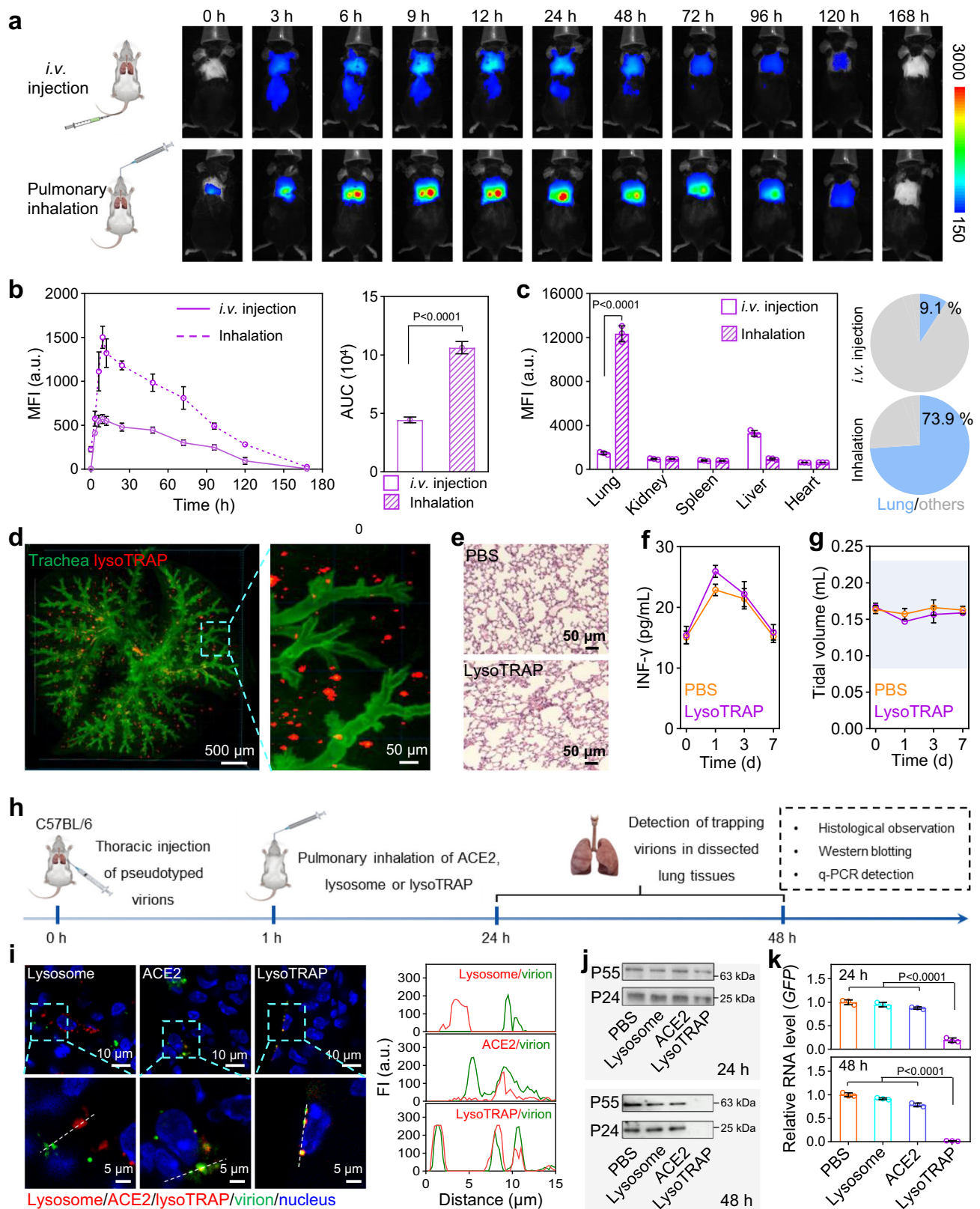
degradation, we directly detected fragments (lower than 10 (kilodalton) kDa) of degraded SARS-CoV-2 via LC-MS, and overlapped these with the 3D crystal structure of SARS-CoV-2 proteins. Taking NSP5 (a well-known main protease participating in processing of viral precursor proteins) for an example, only two fragments (Phe223-Lys236 and Leu282-Arg298) were detected (Fig. 5j), indicating very efficient degradation of NSP5 by h-lysoTRAP.

Considering the plentiful RNases within the h-lysoTRAP, we also investigated the degradation of the SARS-CoV-2 genome. As shown in Fig. 5k, capillary electrochromatography revealed a dynamic genomic degradation process: initially, a clear peak appeared at the 29 kilo nt region, representing an intact viral genome; over time, the viral genome was degraded into smaller fragments of different sizes, with several peaks scattered at different regions (e.g., 22, 18, 16, and 10 kilo

Fig. 3 | In vivo biodistribution and trapping of lysoTRAP. a Schematic for the administration of Cyanine 7 (Cy7)-labeled lysoTRAP via pulmonary inhalation or intravenous (*i.v.*) injection and corresponding in vivo real-time fluorescence images of mice. **b** Corresponding signal profiles of lysoTRAP in **a** and corresponding area under the curve (AUC) calculation, showing the superior bioavailability of lysoTRAP in lungs via pulmonary inhalation. **c** Mean fluorescence intensity (MFI) statistics of the major organs dissected from C57BL/6 mice 9 h after the administration, and corresponding proportion of the lysoTRAP accumulation in lungs. **d** 3D reconstructed light-sheet microscopic image of a lung dissected from a mouse 24 h after pulmonary inhalation of Cyanine 5 (Cy5)-labeled lysoTRAP. The tracheas were labeled with streptavidin-fluorescein isothiocyanate (FITC). **e** H&E images of lung tissue sections after pulmonary inhalation of lysoTRAP or PBS. **f** Analysis of IFN-γ level in the supernatant of lung homogenate after pulmonary inhalation of

lysoTRAP or PBS. **g** The evaluation of lung respiratory function after pulmonary inhalation of lysoTRAP or PBS, assessed as the tidal volume (the volume of air inhaled or exhaled per breath) (the blue background presents the normal range.) **h** Schematic for the detection of in vivo trapping SARS-CoV-2 pseudotyped virions by lysoTRAP in C57BL/6 mice. **i** Representative CLSM images of pseudotyped virion distribution in the lungs at 24 h of post-administration and corresponding quantitative analysis of fluorescence intensity (FI) alongside the white dotted line. **j** WB analysis of viral protein components (P55 and P24) in the lungs, showing the efficient protein degradation by h-lysoTRAP. **k** q-PCR analysis of viral RNA levels (GFP) in lungs. The data in **b**, **c**, **f**, **g**, and **k** represent the mean ± S.D. (*n* = 3 biologically independent mice). Statistical significance was calculated using two-tailed unpaired *t*-test in **b** and **c**, and two-tailed one-way ANOVA with multiple comparison test in **k**. Source data were provided in the Source data file.

nt); at 24 h of post-incubation, the genome was efficiently degraded into very tiny fragments, and almost no viral genome signal was detected. Focusing on the representative viral genes (*e.g.*, *ORF1a*, *ORF1b*, *S*, and *M*), we detected their levels along with the incubation time via q-PCR (Fig. 5l). The levels of these genes shared a time-dependent decreasing profile, with almost no signal being detected after 24 h (Fig. 5m). However, the calculated half-time values of these genes showed a disparity. A strong correlation between the halt-time and length of these genes indicated the gene degradation profile (Fig. 5n): longer gene presented more opportunities for degradation by RNases. All these results thus demonstrated that h-lysoTRAP efficiently degraded authentic SARS-CoV-2 through both protein and genome aspects, which could profoundly reduce the likelihood of escape or continuous infectivity.

h-lysoTRAP-mediated clearance of authentic SARS-CoV-2 on human lung organoids

Having demonstrated the desired trapping functions of h-lysoTRAP in vitro, we evaluated in the position the clearance capacity of h-lysoTRAP against authentic SARS-CoV-2 in human lung organoids, which are known to retain the genetic and epigenetic features of human lung cells and partially recapitulate the 3D cellular environment of the lung (Fig. S21), and have emerged as a powerful tool for SARS-CoV-2 studies[29–31]. Briefly, normal lung tissues adjacent to tumors resected from patients with lung cancer were dissected into tiny pieces and homogenized into single-cell suspension (Fig. 6a). These cells were then seeded into Matrigel containing growth and regulatory factors following a previously described method and ultimately formed lung spheroids, which were utilized for assessing the clearance of authentic SARS-CoV-2 (wild-type and Omicron variant) by h-lysoTRAP[31].

For a comprehensive comparison with the efficacy of the current standard of care against SARS-CoV-2, we additionally engaged two counterparts: EIDD-2801 (molnupiravir: FDA-approved specific medicine servicing as riboside analogs to inhibit viral RNA-dependent RNA polymerase (RdRp) for COVID-19) and RBD-antibody (antibody agent binding with the RBD of S protein of SARS-CoV-2 to inhibit viral infection)[32,33]. As expected, free EIDD-2801 and RBD-antibody groups showed much lower levels of SARS-CoV-2 (wild-type) RNA copies than PBS group (Fig. 6b). Benefiting from the trapping performance, h-lysoTRAP outperformed free EIDD-2801 and RBD antibody group with ~19.1-fold and ~19.7-fold decrease of RNA copies, respectively. Supporting this distinct viral RNA levels, immunofluorescence staining, lactate dehydrogenase (LDH) release detection and morphological observation in the human lung organoids all revealed that h-lysoTRAP completely cleared SARS-CoV-2 virions and efficiently inhibited SARS-CoV-2 infection, over the ameliorative effect detected in the free EIDD-2801 and RBD antibody groups (Fig. 6c-e). Subsequently, we assessed the efficacy of h-lysoTRAP against Omicron variant, and again observed a fantastic capacity of h-lysoTRAP to suppress viral infection with a sharp drop of viral RNA copies and S1 expression, undetectable LDH levels and plump organoids. In contrast, free EIDD-2801 and RBD

antibody (Fig. 6f-i) activity were significantly hindered by this variant. Note that the inhibitory effect of either free EIDD-2801 or RBD antibody between wild-type and Omicron variant appeared obvious discrepancy, but h-lysoTRAP not.

For a holistic perspective, we next performed principal component analysis upon a dimension reduction process of four viral infection indices including viral RNA copies, S1 expression levels, LDH release levels, and the decrease value of organoids volume. The data sources from either free EIDD-2801 or RBD antibody groups were clearly represented as two parted clusters according to the wild-type or Omicron variant (Fig. 6j), indicating their compromised performance against the mutated variant. In contrast, the h-lysoTRAP/wild-type and h-lysoTRAP/Omicron-type cluster not only closely overlapped with each other, but also were clearly separated from PBS, free EIDD-2801, and RBD antibody clusters, revealing the undisturbed clearance capacity of h-lysoTRAP against highly mutated SARS-CoV-2 strains. Accordingly, we observed that the Z scores of h-lysoTRAP were calculated with a very low levels to both wild-type strain and Omicron variant, exceeding that of both free EIDD-2801 and RBD antibody with high levels of strain-unmatched infection indices (Fig. 6k). Such fantastic and insusceptible clearance capacity of h-lysoTRAP should be attributed to the ACE2-mediated trapping performance, whereas traditional care agents against SARS-CoV-2 are sensitive to loss to significant mutations of SARS-CoV-2, compromising the therapeutic effect against SARS-CoV-2 variants. Overall, these findings mirrored our results from the in vivo lysoTRAP analysis and supported the assertion that h-lysoTRAP had a strong capacity to capture, internalize, and degrade either wild-type SARS-CoV-2 or variants, exposing it as a powerful tool against the future co-circulation of multiple SARS-CoV-2 variants.

Extension of lysoTRAP for clearance of H1N1

Encouraged by the effective clearance capacity of lysoTRAP against SARS-CoV-2 and its variants, we aimed to extend our "lysoTRAP" technology for fighting against other viruses. Given that many viruses enter cells through saccharide-receptor interactions, we were particularly interested in exploring the modification of lysosome surface with saccharide-receptor as bait. To this end, we chose H1N1 as another testbed, as it is known to target SA-modified proteins on the membrane of human lung cells[34,35]. To construct SA-engineered lysosomes (lysoTRAP (SA)), we incubated lysosomes with cytidine 5′-monophosphate-N-acetylneuraminic acid (CMP-sialic acid, a substrate for sialyltransferases) and 2,6-sialyltransferase (SIAT1), which achieved the SA modification onto the proteins of the lysosome surface (Fig. 7a).

The highly colocalized signals of SA (labeled by Cy3-conjugated Sambucus nigra lectin) and LAMP-2 in Fig. 7b demonstrated the successful modification of SA on the lysosomes, while almost no change was observed for lysosome morphology (Fig. 7c). Upon further QCM detection, TEM observation, FRET investigation, western blotting analysis, ELISA measurement, and q-PCR analysis, we verified the capture and internalization performance of lysoTRAP (SA) were involved
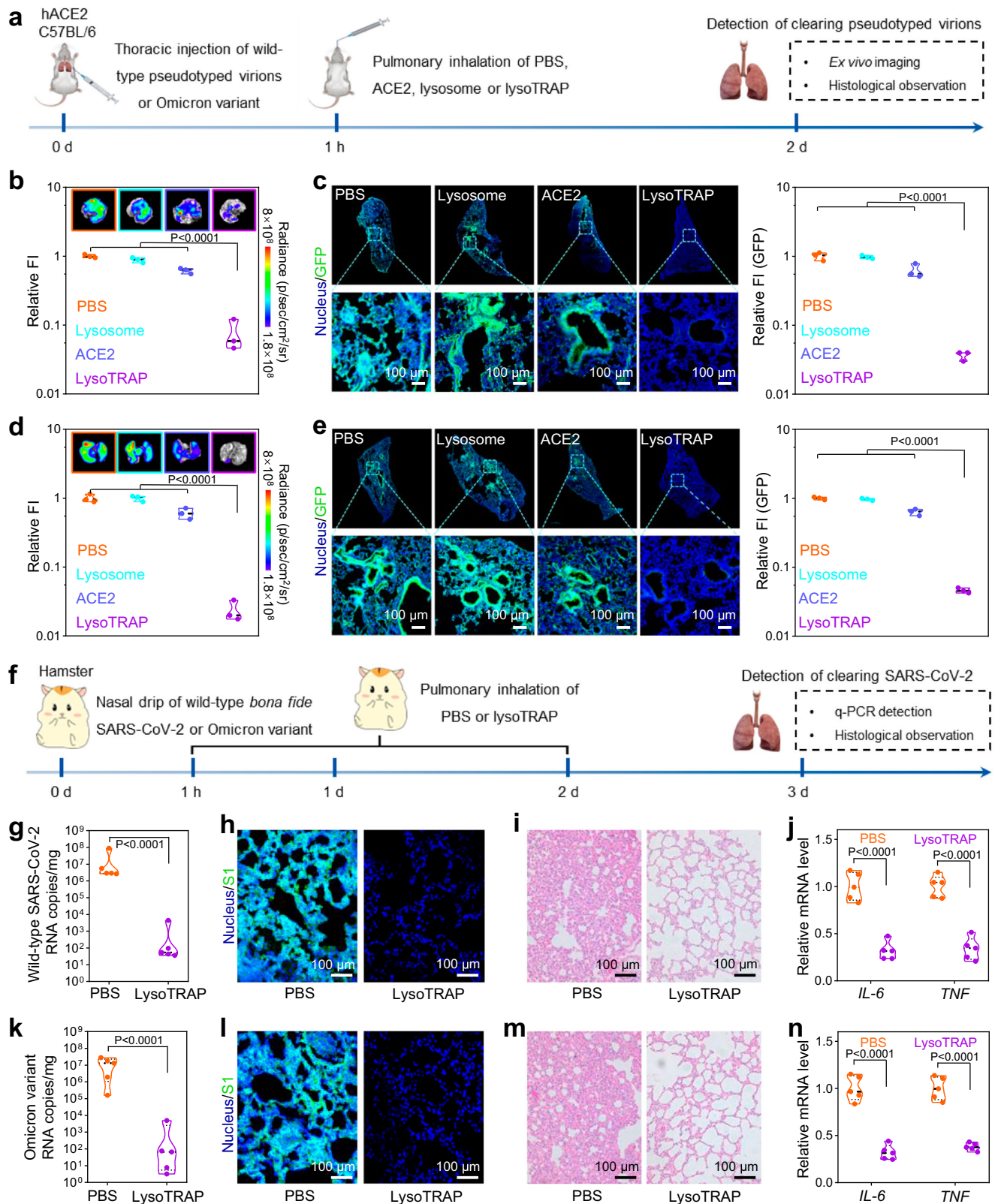
with the SA binding and HA cleavage on the membrane, leading to the efficient degradation of the H1N1-PR8 (Figs. 7d-f and S22-23). Moreover, we evaluated the clearing performance with Madin-Darby Canine Kidney cells (MDCK). Compared to PBS group, lysoTRAP (SA) group showed significant decreases in viral genomic RNA copies and N protein expression of H1N1-PR8 (Figs. 7g and S24), and such a satisfactory in vitro clearance capacity was also found for H1N1-CA07(Fig. S25).

To evaluate efficacy in vivo, mice were challenged intranasally with 1000 TCID50 of H1N1-PR8 or H1N1-CA07 and were administered with either PBS or lysoTRAP (SA) via pulmonary inhalation (Fig. 7h). After 5 d post infection, lung tissues were collected for q-PCR and histological analysis. Compared to PBS group, lysoTRAP (SA) group exhibited a - 4-log reduction in viral RNA copies of both H1N1-PR8 and H1N1-CA07 (Fig. 7i, k), as supported by immunofluorescent staining of

Fig. 4 | In vivo clearance of pseudotyped and authentic SARS-CoV-2 by lyso-TRAP. a Schematic for the detection of in vivo clearance of pseudotyped virions by lysoTRAP in the hACE2 C57BL/6 mouse model. **b** Ex vivo imaging of pseudotyped virion (wild-type) GFP expression (inserted at the top of panel) and corresponding quantitative analysis of GFP fluorescence signals in the lungs dissected from hACE2 C57BL/6 mice after viral inoculation and administration with different treatments. **c** Representative fluorescence images of pseudotyped virion (wild-type) GFP expression in the lung slides and corresponding quantification analysis of the GFP signals. **d, e** Similar data as that presented in **b,c** following infection with the Omicron variant of pseudotyped virions. **f** Schematic for the detection of in vivo clearance of authentic SARS-CoV-2 by lysoTRAP in the hamster model. **g** q-PCR analysis of wild-type SARS-CoV-2 RNA copies in lungs at 3 d. **h** Representative immunofluorescent images of S expression in the lung tissues at 3 d.

i Representative hematoxylin and eosin (H&E) images of the lung tissues at 3 d. The lungs in the PBS group showed abundant infection symptoms (alveolar septal thickening and inflammatory cell infiltration), while those symptoms were almost disappeared in lysoTRAP group. **j** Analysis of inflammatory cytokine (interleukin 6 (*IL-6*) and tumor necrosis factor (*TNF*) mRNA levels in the supernatant of lung homogenate at 3 d via q-PCR detection. Actin was used as the housekeeping gene, and relative gene expression was normalized to the PBS group. **k–n** Similar data as that presented in **g–j** following infection with Omicron variant. The data in **b, c, d**, and **e**, represent the mean ± S.D. (*n* = 3 biologically independent mice). The data in **g, j, k**, and **n** represent the mean ± S.D. (*n* = 5 biologically independent hamsters). Statistical significance was calculated using two-tailed one-way ANOVA with multiple comparison test in **b, c, d**, and **e**, and two-tailed unpaired *t*-test in **g, j, k**, and **n**, respectively. Source data were provided in the Source data file.

lung sections (Figs. S26a, S26c and 6e). Moreover, the lysoTRAP (SA) group showed reduced signs of viral pneumonia in the lung H&E images and lower levels of inflammatory cytokine mRNA in the lung (Figs. 7j, l, S26b and S26d). Additionally, the clearance capacity of human lysoTRAP (SA) iteration (h-lysoTRAP (SA)) against both H1N1-PR8 and H1N1-CA07 was tested in human lung organoids, again showing a significant reduction in viral RNA copies and viral N protein expression (Figs. 7m-o and S27-28). Beyond demonstrating the high efficacy of lysoTRAP (SA) against H1N1 variants, these results also verified the feasibility of using saccharides-receptor as the bait of our "lysoTRAP", which foreboded the feasible clearance of other virus by altering the bait on the lysosome membrane, such as engineering heparin sulfate on the lysosome surface for trapping molluscum contagiosum virus.

Discussion

In summary, our study successfully modified the surface of lysosomes with the viral receptor and demonstrated the effectiveness of our lysoTRAP in capturing, internalizing, and degrading the corresponding virus and its variants in both in vitro and in vivo settings. Utilizing ACE2 as a bait, our lysoTRAP achieved remarkable clearance of pseudotyped and authentic SARS-CoV-2 virions in mouse and hamster infection models. Importantly, similar results were observed in clinically relevant experiments using human lung organoids and a human lysoTRAP iteration, highlighting the translational potential of our lysoTRAP system for developing SARS-CoV-2 therapies. Furthermore, our lysoTRAP was successfully applied to clear H1N1 variants by replacing the protein-receptor ACE2 with the saccharide-receptor SA. These findings strongly support our "TRAP" platform as a novel and versatile virus clearance agent.

While some researchers have also developed vesicles and membrane-coated particles carrying ACE2 proteins for treating COVID-19, it should emphasize that those efforts mainly focused on the binding of vesicles to SARS-CoV-2 via S-ACE2 affinity. The ultra-small size of the vesicles (*e.g.*, ~100 nm for exosomes) and the solid core of the membrane-coated particles are unfavorable for harnessing the potential of viral internalization[36–39], which might fail to completely isolate the virus from host cells. More importantly, the SARS-CoV-2 trapped within our designed lysoTRAP was efficiently degraded by the lysosomal proteases and RNases. The likelihood of viral escape or continued infectivity was thus profoundly reduced as compared with other reported anti-SARS-CoV-2 vesicles and particles. In addition, we demonstrated that lysoTRAP could be administered directly to the lungs via a pulmonary inhalation route, which increased the accumulation and bioavailability of lysoTRAP in the respiratory track. This seemed like a more sensible administration route as compared to the *i.v.* injection used in many previous studies, as SARS-CoV-2 is a respiratory pathogen aiming to infect the lungs, and this choice had the superiorities of efficient accumulation and high bioavailability.

As a therapeutic for treating SARS-CoV-2, our lysoTRAP also hold unique advantages. Compared with other agents available as current

standard treatment, which mostly targeted the S protein and loose efficacy due to frequent mutations of SARS-CoV-2 S protein[40,41], our lysoTRAP exerted the same performance against nine SARS-CoV-2 variants. This makes sense, as the working principle for lysoTRAP's recognition of the target virus is the ACE2 protein, which is understood as an indispensable factor for the entry of SARS-CoV-2 into host cells. The ideal administration time for this therapeutic may be at the first sign of viral infection symptoms or during a mild viral infection. In this situation, the virus at a low burden can be eliminated by our lysoTRAP. Considering the outstanding performance of our lysoTRAP at a low dose against authentic SARS-CoV-2 in the hamster model, we can also expect an extended effective treatment of lysoTRAP in the later stages of infection with an increased dose and frequency. Given that SARS-CoV-2 infection can induce severe pulmonary inflammation, it seems likely that a combination intervention comprising lysoTRAP alongside an anti-inflammatory drug could be beneficial. On this point, it bears mention that lysosomes are known to have multiple compartments (*e.g.*, hydrophilic inner cavity and hydrophobic membrane layer), which can be harnessed to accommodate anti-inflammatory drugs.

Several issues need addressing regarding the design of future iterations of this "TRAP" platform. For example, we constructed the "TRAP" platform based on blood macrophages. In terms of lysoTRAP preparation, it is conceivable to render yet-more-straightforward strategy. Instead of the DSPE-PEG-NTA-Ni chelation strategy we demonstrated in the present study, for example, one end of a lysosomal localization signal peptide (*e.g.*, LAMP-2 signal peptide GYEQF) can be fused to the C-terminal end of the ACE-2 protein[42], and then the corresponding gene can be imported into cells to express the ACE2 protein on the surface of lysosomes. For SA decoration, we may be able to express 2,6-siayltransferase in the cytoplasm of macrophage via gene transfection, which can directly modify SA on the lysosomal membrane surface upon the existence of GMP-SA in cytoplasm. Attention should also be given to the optimization of the internal components of lysosomes. For example, gene editing of cells should enable selective augmentation of lysosomal enzymes (proteases, nucleases, phospholipases, etc.), which could provide yet-higher efficiency of lysosomal degradation to trapped particles.

In the advent of clinical implementation of this strategy, the production scale of lysosomes is an essential issue. Looking beyond blood macrophages, it may be possible to use other cell types (e.g., stem cells) that have higher proliferation and multipotent differentiation capacity as the source of lysosomes to improve production scale. For cell culture, cell expansion through 3D culture with appropriate cell growth scaffolds (such as microcarriers) can be considered as a useful strategy for scalable and efficient production of cells. Moreover, essential properties of lysoTRAP should be carefully examined in the quality control process, such as size, zeta potential, inner pH, surface/functional markers, cathepsin activity, RNase activity, and ACE2 abundance. Additionally, the formulation of freeze-drying protective additives deserves optimization to further prolong the storage time of lysoTRAP, such as optimizing the ratio of trehalose and mannose.
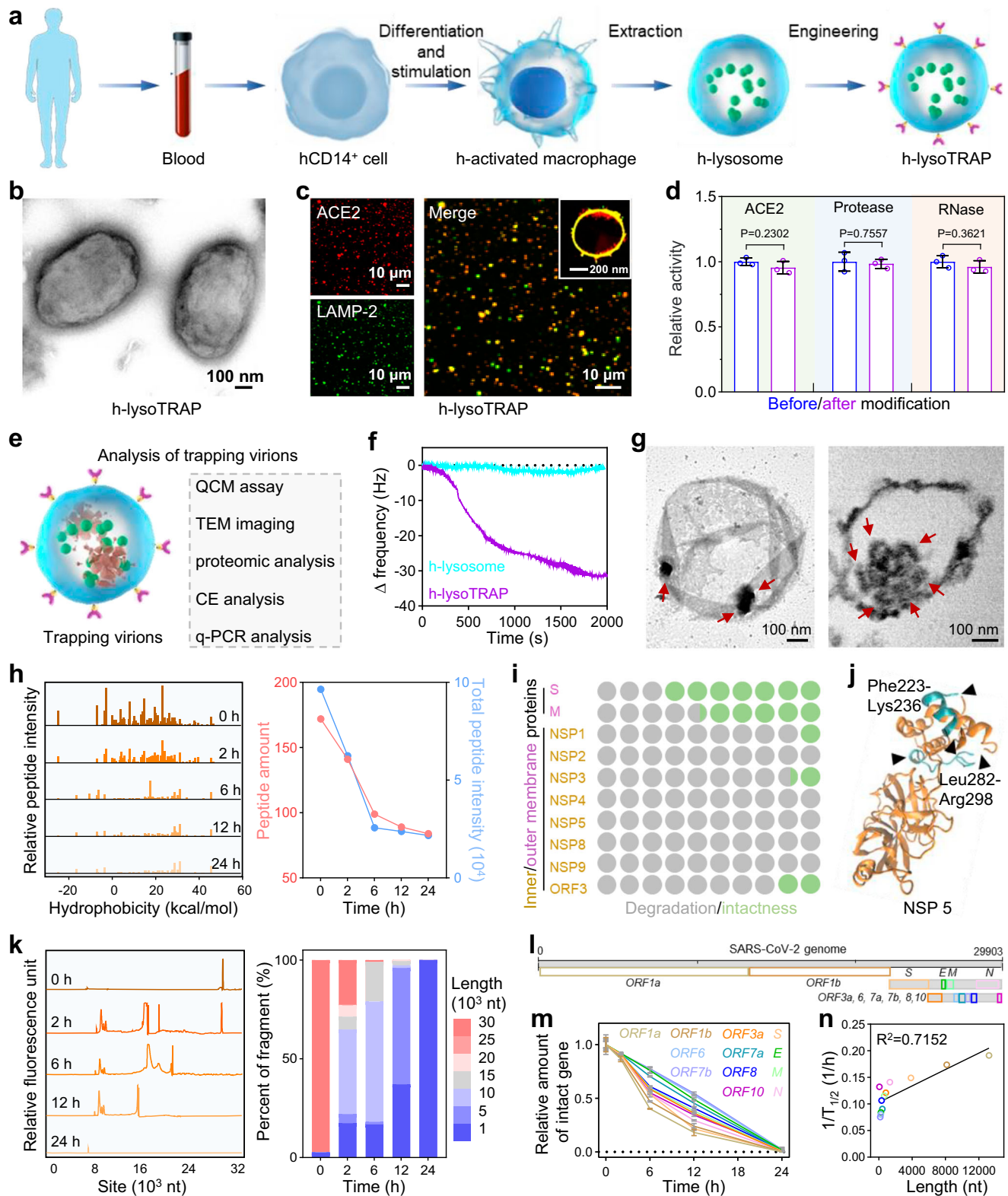
In the aspect of translational potential, the lysoTRAP have good biocompatibility, since we constructed the lysoTRAP based on natural biological materials such as the ACE2 protein, SA and lysosome. From an application perspective, lysoTRAP can be conveniently lyophilized without damage or loss of activity, thereby facilitating clinical use in an acute setting. Moreover, almost no human leukocyte antigen (HLA) molecules were detected on the external surface of lysoTRAP (Fig. S16)[43,44], thereby decreasing the chance of immune incompatibility

between the donor and recipient. This attribute should expand the source of suitable donor cells, as it seems that non-allogenic lysoTRAP can be prepared from allogeneic or even xenogeneic sources. Additionally, it can be envisioned that our lysosome-based "TRAP" strategy can be extended beyond the straightforward application scenario as treatment described here. Considering the half-time of lysoTRAP in the lungs is approximately 80 hours, we can also expect the possibility of using our lysoTRAP as a prophylactic measure to provide protection

Fig. 5 | Construction of human lysoTRAP and the performance of trapping authentic SARS-CoV-2 in vitro. a Schematic for the construction of human lyso-TRAP (h-lysoTRAP). **b** TEM image of h-lysoTRAP. **c** CLSM and STED images (inserted at the upper right corner) of h-lysoTRAP, showing the successful anchorage of ACE2 to the h-lysoTRAP membrane. **d** Enzymatic activities of ACE2, proteases and RNases in lysosomes before and after ACE2 anchorage to h-lysosomes. **e** Schematic for trapping SARS-CoV-2 by h-lysoTRAP and corresponding investigation methods, including QCM assay, TEM imaging, proteomic analysis, capillary electrophoresis (CE) analysis and q-PCR analysis. **f** QCM analysis of the interaction between authentic SARS-CoV-2 virions (wild-type) and h-lysoTRAP (h-lysosomes). **g** TEM imaging and corresponding TEM section observation of h-lysoTRAP after a 4-hour co-incubation with SARS-CoV-2 virions. The internalized virions were indicated by red arrows in h-lysoTRAP. **h** Peptide fingerprints of SARS-CoV-2 proteins identified by LC-MS after h-lysoTRAP incubation for indicated time points. The right panel showed the corresponding quantitative analysis of the amount and total intensity of identified peptide, highlighting the expected h-lysoTRAP-mediated decrease of

SARS-CoV-2 proteins. **i** Degradation proportion analysis of representative viral proteins after a 24-hour co-incubation with h-lysoTRAP based on the proteomics data. The degradation proportions of each viral protein were normalized according to the PBS group. **j** Detection of residual peptides of NSP5 after a 24-hour co-incubation with h-lysoTRAP via proteomic analysis. For visualization, the detected peptides (marked with cyan) were overlapped upon the NSP5 crystal 3D Structure. **k** CE analysis of authentic SARS-CoV-2 genome and corresponding distribution analysis of viral genome and fragments, showing a dynamic degradation process on viral genome scale. **l** Schematic for the authentic SARS-CoV-2 genome. **m** Degradation profiles of representative authentic SARS-CoV-2 genes with h-lysoTRAP treatment based on q-PCR data. **n** Correlation analysis between degradation half-time and length of representative authentic SARS-CoV-2 genes. The R^2 values reflect Pearson's correlation analysis. The data in **d, m**, and **n** represent the mean ± S.D. ($n = 3$ biologically independent experiments). Statistical significance was calculated using two-tailed unpaired t-test in **d**. Source data were provided in the Source data file.

for a few days. Therefore, our lysoTRAP may serve as a new tool to protect individuals who are exposed to high-risk environments (e.g. hospitals or crowded public transport).

Methods

Study approval

The mouse study was performed in strict accordance with the Regulations for the Care and Use of Laboratory Animals and Guideline for Ethical Review of Animal (China, GB/T 35892-2018). The animal protocol was reviewed and approved by the Animal Ethics Committee of the Institute of Process Engineering (approval ID: IPEAECA2021013).

The hamster study was performed in strict accordance with the Regulations for the Care and Use of Laboratory Animals and Guideline for Ethical Review of Animal (China, GB/T 35892-2018). The animal protocol was approved and conducted in accordance with the institutional guidelines of the Peking Union Medical College Animal Care and Use Committee (approval ID: DWSP202207004).

The human studies were approved by the Biomedical Research Ethics Committee of Peking University First Hospital (approval ID: No.2018-135 and No.2021-486) and written informed consent was obtained from health donor.

Reagents and materials

Anti-human ACE2 antibody (ab272500), Anti-LAMP-2 antibody (ab25631), Anti-LAMP-1 antibody (ab24170), Anti-S1 antibody (ab281311), Anti-AQP5 antibody (ab92320), Anti-SFTPC antibody (ab90716), Anti-N protein of H1N1 antibodies (ab104870), Goat anti-rabbit secondary antibody-Alexa Fluor® 488 (ab150077), Rabbit anti-goat secondary antibody-Alexa Fluor® 647 Abcam (ab150083), Anti-HIV1 p55-p24-p17 antibody (ab309159), Anti-human ACE2 antibody (ab108252), Anti-LAMP-2 antibody (ab19947), Anti-S2 antibody (ab283913), and Anti-HA antibody (ab281948) were purchased from Abcam. Alexa Fluor® 647 anti-mouse MHC-I Antibody (111512), Alexa Fluor® 488 anti-mouse MHC-II Antibody (114407), FITC anti-mouse/human CD11b Antibody (101206), PE anti-mouse F4/80 Antibody (111604), Brilliant Violet 510™ anti-mouse Ly-6G Antibody (127633), and Alexa Fluor® 700 anti-mouse Ly-6C Antibody (128024) were purchased from Biolegend. Human ACE2 and RBD antibody were purchased from Sino Biological. EIDD-2801 was purchased from MedChemExpress. Cytochalasin B, puromycin, FITC, sodium fluorescein, Agarose (Low melting gel) and streptavidin-FITC was purchased from Solarbio Life Sciences. Lysosome Extraction Kit was purchased from Bestbio. Enzyme-linked immunosorbent assay (ELISA) kits for cytokines (IFN-γ, IL-6, and TNF), Acid Protease Activity Detection Kit were purchased from Solarbio Life Sciences. RNAeasy™ Viral RNA Isolation Kit with Spin Column, ACE2 Activity Fluorometric Assay Kit, and BeyoFast™ SYBR Green One-Step qRT-PCR Kit were purchased from Beyotime Biotechnology. One Step

PrimeScript q-PCR Kit was purchased from TCI. All primers were purchased from Sangon Biotechnology. 1,1'-Dioctadecyl-3,3,3', 3'-Tetramethylindodicarbocyanine,4-Chlorobenzenesulfonate Salt (DiD), Cyanine7 NHS ester (Cy5-SE) and Cyanine5 NHS ester (Cy5-SE) were purchased from FANBO biochemicals. OrganoPro™ Huamn Lung Organoids Culture Kit was purchased from K2ONCOLOGY. Matrigel™ was purchased from Coring/BD. Penicillin-Streptomycin, Trypsin-EDTA, and Dulbecco's modified Eagle medium (DMEM) high supplemented were purchased from Biological Industries. Pseudo-type SARS-COV-2 (wild-type) were purchased from Langmiao Biotechnology.

Cell lines

MDCK (catalog no. CL-0154) was purchased from Procell Life Science&Technology Co., Ltd (Wuhan, China). ACE2-OE HEK-293T (catalog no. BFN60700110A) was purchased from Shanghai Qingqi technology Co., Ltd (Shanghai, China). ACE2-OE HEK293T cells were cultured in Dulbecco's modified Eagle medium (DMEM, high glucose; BI) supplemented with 100 U/mL of Penicillin-Streptomycin solution, and 10% fetal bovine serum (FBS, GIBCO) in a 5% CO_2 environment at 37 °C. Mice peritoneal macrophages were harvested from stimulated female C57BL/6 mice according to a typical protocol and cultured under standard conditions[45]. Briefly, mouse peritoneal macrophages were collected from 8-10 week-old C57BL/6 mice by peritoneal lavage with 10 ml of phosphate-buffered saline, centrifuged at 500 g for 10 min, and cultured in RPMI 1640 medium containing 10% (v/v) fetal bovine serum (FBS), 2 mmol L-glutamine, 100 U/mL penicillin, and 100 g/mL streptomycin. Hamster peritoneal macrophages were harvested from female hamsters (8 week-old) with same above-mentioned procedure of mice, excepting for 50 ml of PBS for the peritoneal lavage. Human macrophages were generated from the peripheral blood mononuclear cells (PBMCs) by induced differentiation[46]. Briefly, PBMCs were isolated from peripheral blood of HLA-A2+ health donor by Ficoll-Paque density gradient separation, and then CD14+ cells were isolated from PBMCs using CD14 Microbeads and cultured in the RPMI-1640 medium containing 20% human serum and 1% penicillin/streptomycin in the presence of recombinant GM-CSF (50 ng/mL).

Animals

Female C57BL/6 mice (8 weeks old) were purchased from Beijing Vital River Laboratories and female human ACE2 C57BL/6 mice (8 weeks old) were purchased from Gempharmatech Co.,Ltd. The mice were housed in an environmentally controlled room (23 °C, with 55 ± 5% humidity and under a 12 h–12 h light–dark cycle).

Female hamsters (8 weeks old) were purchased from Beijing Vital River Laboratories and were housed on the Animal Center of the Peking Union Medical College for SARS-CoV-2 study. The hamsters were housed in an environmentally controlled room (23 °C, with 55 ± 5%
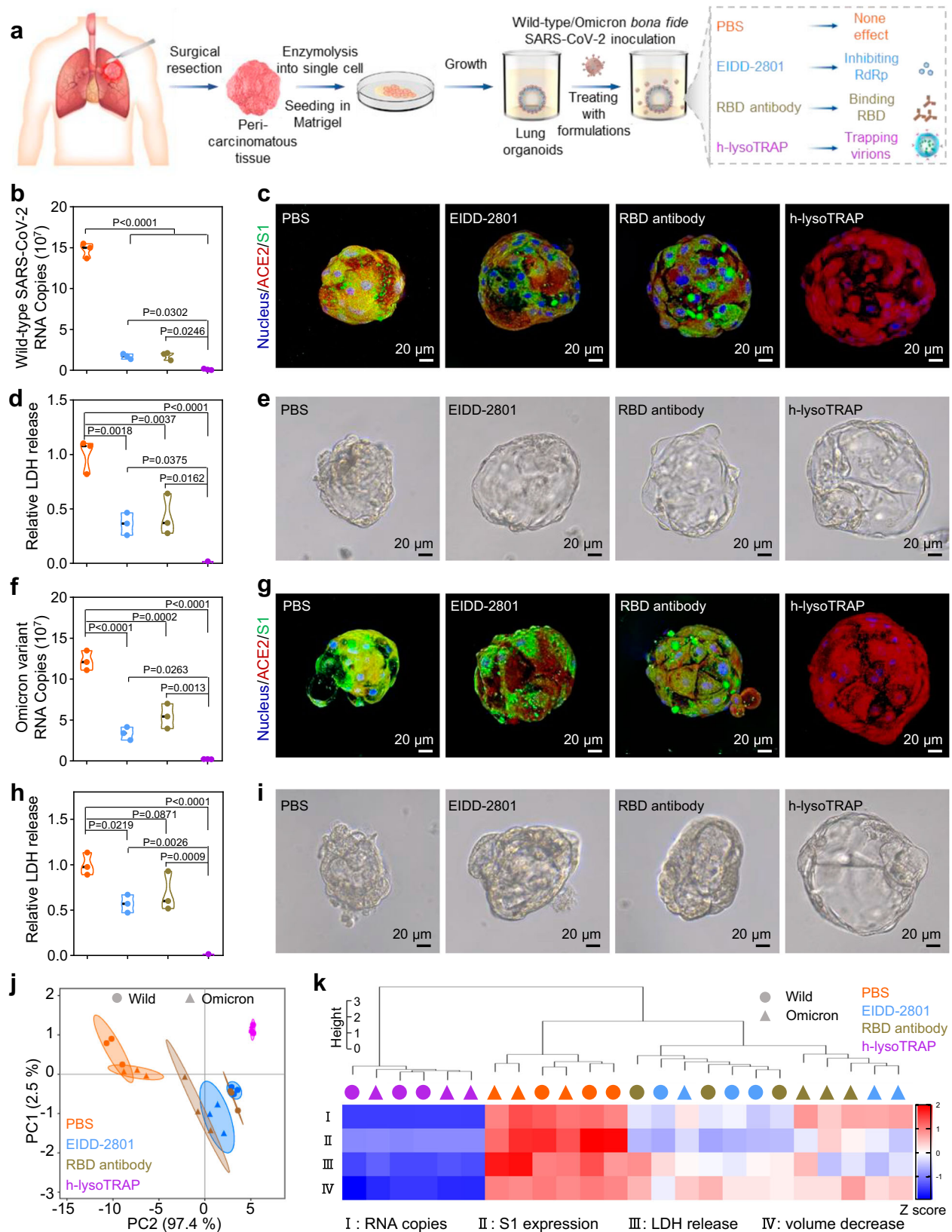
humidity and under a 12 h–12 h light–dark cycle). All animals were randomly divided into various groups for subsequent experiments.

Virus

In the study, ten pseudotyped SARS-CoV-2 were utilized including wild-type pseudotyped SARS-CoV-2 and nine pseudotyped SARS-CoV-

2 variants. The wild-type pseudotyped SARS-CoV-2 was purchased from Langmiao Biotechnology, and was prepared as lentiviral vector by using a pseudotyped virus packaging system of human immuno-deficiency virus (HIV) with expressing the S protein at the capsid membrane surface. Nine pseudotyped SARS-CoV-2 variants were gifted from Professor Youchun Wang of Institute for Biological Product

Fig. 6 | h-lysoTRAP-mediated clearance of authentic SARS-CoV-2 on human lung organoids. a Schematic for the construction of human lung organoids and anti-infection experiment on organoid model. Lung cells (isolated from normal lung tissues adjacent to tumors derived from resection surgeries) were seeded into Matrigel containing known growth and regulatory factors to induce lung spheroids. 1 d after inoculation with 100 TCID50 authentic SARS-CoV-2 and treatment with different formulations, the lung spheroids were collected for q-PCR analysis, immunofluorescence analysis and lactate dehydrogenase (LDH) release detection. In these formulations, free EIDD-2801 (molnupiravir) can bind with RNA-dependent RNA polymerase (RdRp) to inhibit SARS-CoV-2 infection and have been FDA-approved specific medicine for COVID-19. Free RBD antibody can bind with the RBD area of S protein of SARS-CoV-2 to inhibit SARS-CoV-2 infection. The concentration of free EIDD-2801 and RBD antibody was selected to match the amount of ACE2 present on the membrane of the h-lysoTRAP. **b** q-PCR analysis of wild-type SARS-CoV-2 RNA copies in human lung organoids, showing the efficient virion clearance and efficiently inhibited viral infection by h-lysoTRAP in human lung organoids. **c** Representative immunofluorescence images of wild-type SARS-CoV-2 infection, visualized by S protein expression in human lung organoids. **d** Relative LDH release from human lung organoids after viral inoculation and formulation treatment. **e** Representative photos of the organoids after viral inoculation and formulation treatment. **f–i** Similar data as presented in **b–e** following infection with Omicron variant. **j** Principal component analysis showing the viral infection profiles (four infection indices) across eight groups. Each dot represents a human lung organoid; the colors of the dot denote the groups; and the ellipses show the distribution of the groups. **k** Visualization of indices of viral infection among the eight groups. Data were normalized for plotting. The data in **b, d, f**, and **h** represent the mean ± S.D. (*n* = 3 biologically independent experiments). Statistical significance was calculated using two-tailed one-way ANOVA with multiple comparison tests in **b, d, f**, and **h**. Source data were provided in the Source data file.

Control, National Institutes for Food and Drug Control (NIFDC), and WHO Collaborating Center for Standardization and Evaluation of Biologicals, Beijing, China. These variants with S protein mutations were prepared using a pseudotyped virus packaging system of vesicular stomatitis virus (VSV)[47], including the D614G strain, three variants of interest (VOI) and five variants of concern (VOC).

In the experiments of trapping authentic SARS-CoV-2 in vitro and clearing authentic SARS-CoV-2 on human lung organoid model, wild-type authentic SARS-CoV-2 (SARS-CoV-2/human/CHN/CN1/2020, GenBank number MT407649.1) and SARS-CoV-2 Omicron variants were utilized following the institutional biosafety guidelines of biosafety level 3 (BSL3) laboratory by the Sinovac Life Sciences Co., Ltd. In the experiment of clearing authentic SARS-CoV-2 on hamster model, wild-type strain (SARS-CoV-2-KMS1/2020/GenBank accession number: MT226610.1) and Omicron strain (CCPM-B-V-049-2112-18) were utilized following the institutional biosafety guidelines of BSL3 laboratory by the Institute of Medical Biology, Peking Union Medical College, Chinese Academy of Medical Sciences, Kunming, China.

Preparation of lysoTRAP
Activation of primary macrophages. Primary macrophages (mouse-derived, hamster-derived and human-derived) were cultured in 1640 medium containing 1 ng/mL lipopolysaccharide (LPS) for about 48 h, resulting in the activation of primary macrophages.

Isolation of lysosomes. The preliminary lysosomes were obtained from above primary macrophages by using the Lysosome Extraction Kit (Bestbio) according to the manufacturer's instructions. In brief, the activated primary macrophages were re-suspended in reagent A at 4 °C for 10 min, followed by a homogenization to destroy cell structure. Then, the homogenate was successively centrifuged at 1000 g for 5 min, 3000 g for 10 min, 5000 g for 10 min and 20,000 g for 20 min to isolate lysosomes. The lysosome precipitate was re-suspended in reagent B and was further purified by centrifugation. Then, we further purified lysosomes with immune magnetic beads via immunization method, in which the obtained lysosomes were successively processed with capture of LAMP-1 Dynabeads (anchored with LAMP-1 antibody (ab24170, Abcam), adsorption under magnetic field, and elution via LAMP-1 peptide (ab25744, Abcam) for the purity of lysosomes.

Modification of lysosome. The lysosomes were mixed with DSPE-PEG-NTA-Ni at 37 °C for 1 h for anchoring the NTA-Ni. Then the mixture was centrifuged to remove free DSPE-PEG-NTA-Ni and ACE2-His tag fusion protein was added into the lysosome solution. After 1 h incubation, the free ACE2 was removed by centrifuging and lysosomes modified with ACE2 protein (lysoTRAP) were obtained. The ACE2 protein utilized in the study was a commercial product and purchased from SinoBiological company (cat: 10108-H08H). This recombinant human ACE2 protein was produced by human HEK293T cells, in which the transferred DNA encoded extracellular domain of human ACE2 (Met1-Ser740) with a polyhistidine tag at the C-terminus.

Characterizations of the lysosomes with or without LPS stimulation.
The morphology of lysosomes isolated from macrophages stimulated with or without LPS was observed using transmission electron microscope (TEM) (JSM-6700, JEOL, Japan). Protein concentration of these lysosomes was determined by Micro BCA Protein Assay Kit (PI23235, Thermo Scientific). For deep investigation, LC-MS based proteomics analysis was conducted by Q Exactive™ Hybrid Quadrupole-Orbitrap™ Mass Spectrometer with associated software (Thermo Proteome Discoverer, version 2.5.0.400) to analyze the hydrolase amount in the lysosomes with or without LPS stimulation. Specific steps were as follows

(1) Sample preparation. The lysosomes were obtained from macrophages with or without LPS stimulation by using the Lysosome Extraction Kit (Bestbio) according to the manufacturer's instructions. The proteins of each sample were extracted from lysosomes by protein extraction solution containing 8 M urea.

(2) Protein Processing. A 100 μg aliquot of above extracted proteins was first subjected to reduction via incubating with 200 mM dithiothreitol (DTT) solution at 37 °C for 1 h. Then, protein samples were digested into small peptides by incubating with trypsin (trypsin: protein =1:50) at 37 °C overnight.

(3) LC-MS Analysis. LC-MS Analysis of above-obtained tryptic peptides was conducted on a quadrupole Orbitrapmass spectrometer (Orbitrap Exploris™ 480, Thermo Fisher Scientific, Bremen, Germany) coupled to an EASY nLC 1200 ultra-high-pressure system (Thermo Fisher Scientific) via a nano-electrospray ion source. Briefly, 500 ng of above-obtained tryptic peptides were loaded on a 25 cm column packed using ReproSil-Pur C18-AQ 1.9-μm silica beads and eluted over a 60 min gradient of Acetonitrile and Formic acid. Spectra were acquired with an Orbitrap Exploris™ 480 Mass Spectrometer (ThermoFisher Scientific) with FAIMS Pro™ Interface (ThermoFisher Scientific).

(4) Data analysis. All RAW files were analyzed using the Proteome Discoverer suite (version 2.4, Thermo Fisher Scientific). MS spectra were searched against the UniProtKB mouse proteome database to identify the peptides. Percolator was used to filter spectral matches and peptides with a false discovery rate (FDR) of less than 1%. After spectral assignment, identified peptides were assembled into proteins and were further filtered based on the combined probabilities of their constituent peptides to a final FDR of 1%.

(5) Quantitation and normalization. The amounts of each identified proteins were quantitated by the amount and intensity of corresponding peptides identified in LC-MS analysis. The same amounts of tryptic peptides applied in LC-MS analysis ensured the normalization between each sample in the proteomics.
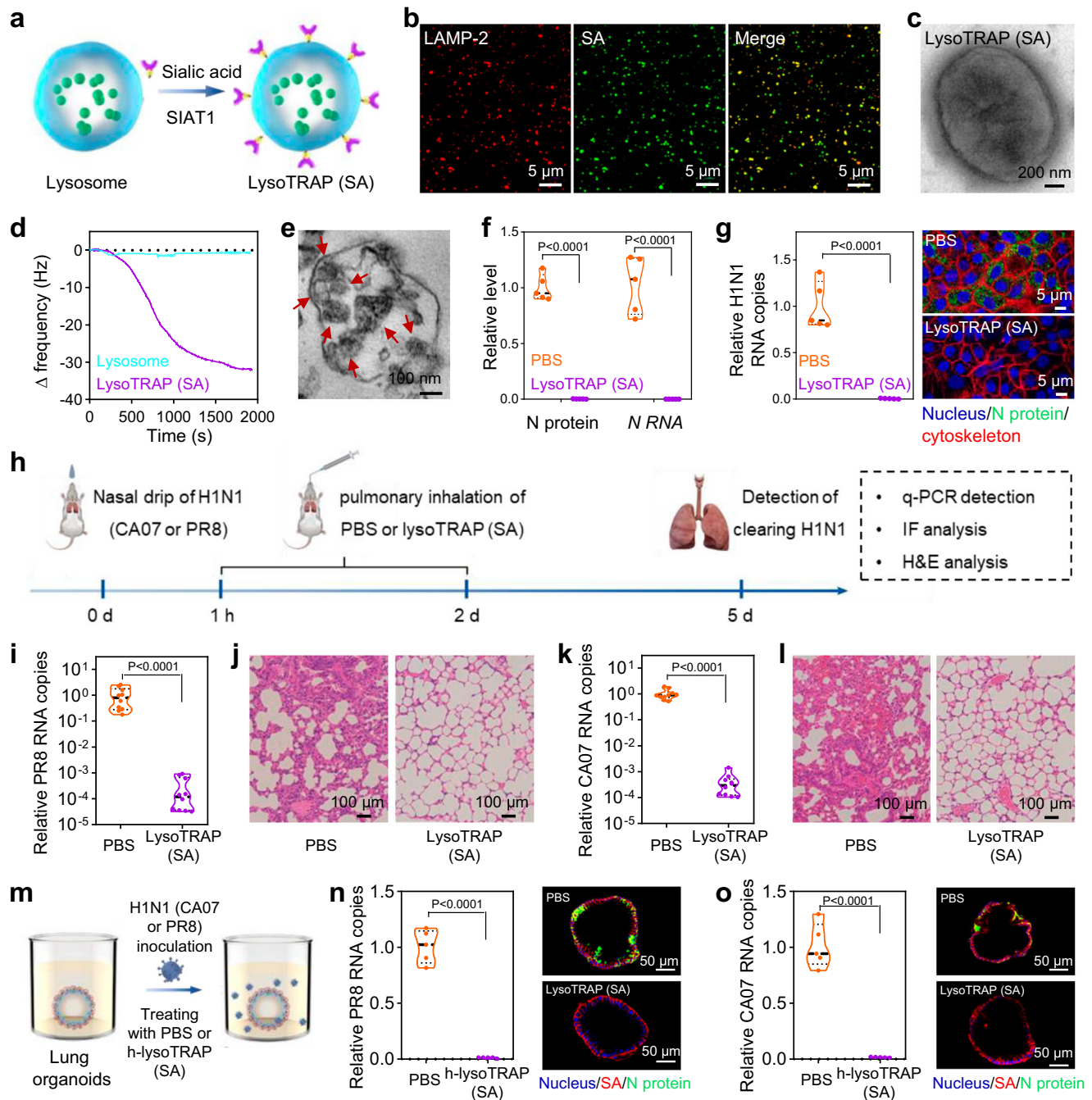
Fig. 7 | Extension of lysoTRAP for clearance of H1N1 in vitro, in vivo and on human lung organoids. a Schematic for the construction of sialic acid (SA) engineering lysosome (lysoTRAP (SA)). Upon 2,6-siayltransferase (SIAT1) and Cytidine 5′-monophosphate-N-acetylneuraminic acid (CMP-SA), the surface of the lysosome was modified with SA, which served as a H1N1 entry-point. **b** CLSM images of lysoTRAP (SA). **c** TEM lysoTRAP (SA) showing the typical lysosome morphology. **d** QCM analysis of the interaction between H1N1-PR8 virions and lysoTRAP (SA). **e** TEM imaging of lysoTRAP (SA) after a 4-hour co-incubation with H1N1-PR8 virions. The internalized H1N1-PR8 virions were indicated by red arrows in lysoTRAP (SA). **f** ELISA measurement of viral N protein level and q-PCR analysis of H1N1-PR8 mRNA expression after a 24-hour incubation with lysoTRAP (SA). **g** q-PCR analysis of H1N1-PR8 mRNA expression (left) and representative CLSM images of N protein expression (right) in MDCK cells upon treatment with PBS or lysoTRAP (SA). **h** Schematic for the detection of in vivo clearance of H1N1 virions by lysoTRAP (SA)

in C57BL/6 mice. **i** q-PCR analysis of H1N1-PR8 mRNA levels in the lung tissues. **j** Representative H&E images of the lung tissue after H1N1-PR8 infection. **k**–**l** Similar data as that presented in **i,j** following infection with H1N1-CA07. **m** Schematic for the anti-infection experiment on human lung organoid model. 1 d after inoculation with 100 TCID50 H1N1-CA07 or H1N1-PR8 and treatment with PBS or h-lysoTRAP (SA), the human lung organoids were collected for q-PCR analysis and immunofluorescence analysis. **n** q-PCR analysis of H1N1-PR8 RNA copies and representative immunofluorescence images of N protein of H1N1-PR8 in human lung organoids. **o** Similar data as that presented in **n** following infection with H1N1-CA07. The data in **f, g, n,** and **o** represent the mean ± S.D. ($n = 5$ biologically independent experiments). The data in **i** and **k** represent the mean ± S.D. ($n = 10$ biologically independent mice). Statistical significance was calculated using two-tailed unpaired t-test in **f, g i, k, n,** and **o**. Source data were provided in the Source data file.

Characterizations of lysoTRAP. The particle sizes and zeta potential of lysoTRAP were analyzed by Nanoparticle Tracking Analysis (NTA, Mastersizer 2000, Malvern Instruments Ltd, UK). The morphology of lysoTRAP was observed using TEM (JSM-6700, JEOL, Japan). To verify successful ACE2 anchorage on the surface of lysoTRAP, immunofluorescent staining was performed. LysoTRAP were successively labeled with ACE2 fluorescent antibody and LAMP-2 fluorescent antibody, and observed by using confocal laser scanning microscopy (CLSM, A1/SIM/STORM, Nikon, Japan). The amount of ACE2 molecule per lysoTRAP was determined by enzyme-linked immunosorbent assay (ELISA). In brief, 96-well plates (Corning) were coated with above unmodified ACE2 protein supernatant overnight at 4 °C in coating buffer, and blocked in 5% bovine serum albumin in PBS for 2 hours at 37 °C. Then the plates were successively incubated with 100 μL of rabbit anti-ACE2 with a 1:10000 dilution at 37 °C for 0.5 h, followed the incubation by HRP-conjugated goat anti-rabbit secondary antibody at 37 °C for 0.5 h. Plates were washed quintic with 1× PBS containing 0.05% Tween-20 (PBST) and pigmented with 3,3′,5,5′-tetramethylbenzidine for 10 min at room temperature, and the reaction was stopped with 2 M H_2SO_4. The absorbance at 450 nm was measured by a microplate reader (Tecan Infinite M200). The enzymatic activities of ACE2, Cathepsin L, Cathepsin B. total protease and RNase in intact lysosome or lysoTRAP were detected by ACE2 Activity Fluorometric Assay Kit (P0139S, Beyotime, China), Cathepsin L Assay (ab270774, Abcam), Cathepsin B Assay (ab270772, Abcam), Acid Protease Activity Detection Kit (BC2280, Solarbio, China), and RNase Activity Fluorometric Assay Kit (P0347S, Beyotime, China), respectively. The acid environment in lysosomes was determined by a lysosomal acid indicator purchased from TongRen Chemical (L264, China). To obtain the lysates of lysosome and lysoTRAP, repetitive freeze-thawing was used to gently break the membrane of lysosome and lysoTRAP. The enzymatic activity of the Furin on the external surface of lysosomes or lysoTRAP was detected by Furin Protease Assay Kit (Bioscience, 78040). The lyophilized lysoTRAP was obtained by using freeze drying technique with the freeze-drying protective additives (50 mM trehalose and 100 mM mannitol).

Programmed performance of lysoTRAP in capturing, internalizing, and degrading pseudotyped SARS-CoV-2 virions in vitro

LysoTRAP capturing pseudotyped SARS-CoV-2 virions. To verify the specific capture performance of lysoTRAP to SARS-CoV-2 pseudotyped virus, quartz crystal microbalance (QCM) experiment was conducted according to a reported protocol[48]. Briefly, equivalent amounts of lysosomes, lysoTRAP, lysoTRAP+ACE2-Ab (lysoTRAP pretreated with ACE2 antibody), lysoTRAP+LAMP-2-Ab (lysoTRAP pretreated with LAPM-2 antibody) were respectively flowed out the Au chip, and the effluent was collected for NTA analysis, obtaining the accurate amount remained on chip. Then, the PBS was continuously pumped to balance the baseline, the effluent was also collected for NTA analysis, obtaining the accurate amount of lysosomal material on the chip. Of note, equivalent amounts of lysosomal material were retained on the chip between different groups. Next, pseudotyped SARS-CoV-2 virions or control virions (pseudotyped virions without S protein) were continuously flowed through the chip until the frequency curve reached a plateau. Finally, PBS flowed to remove any nonspecific binding. In this process, the collected electrical signals (mainly frequency) respond to weight changes on the chip. It should be noted that the captured virions could be further internalized by lysoTRAP, which would not induce the mass change on chips. Therefore, the weight change could be utilized to indicate the relative amounts of virions captured by lysoTRAP/lysosomes.

LysoTRAP internalizing pseudotyped SARS-CoV-2 virions. LysoTRAP and pseudotyped SARS-CoV-2 virions were incubated with Cyanine5 NHS ester (Cy5-SE) and BODIPY (lipophilic micro-molecule fluorescent dye with good stability under acidic condition, inserted into the phospholipid membrane) at 37 °C for 1 h, respectively, and purified to remove free Cy5-SE and BODIPY via ultrafiltration. Then, 10 μg Cy5-labeled lysoTRAP was mixed with 5×10^8 TU BODIPY-labeled pseudotyped SARS-CoV-2 virions at a rate of 1:5 (lysoTRAP: pseudotyped virion) (total volume: 1 mL). Then, we captured the dynamic internalizing process about the signal from BODIPY-labeled pseudotyped virion into Cy5-labeled lysoTRAP in a real time via CLSM (A1/SIM/STORM, Nikon, Japan). To further verify the performance of internalizing the SARS-CoV-2 pseudotyped virions inside lysoTRAP, the lysoTRAP was incubated with pseudotyped virion at 37 °C for 1 h and observed by stimulated emission depletion microscopy (STED, SP8, Leica) and TEM (JSM-6700, JEOL, Japan).

To explore the internalization mechanism of SARS-CoV-2 by lysoTRAP, Fluorescence Resonance Energy Transfer (FRET) analysis was conducted. Briefly, lysosome or lysoTRAP lysosomal samples (naked lysosomes, lysoTRAP and lysoTRAP with Furin inhibitor (1 nM chloromethylketone)) were labeled by Cy7-SE (excitation/emission: 755/785 nm), and pseudotyped SARS-CoV-2 virions were labeled by Cy5.5 (excitation/emission: 673/715 nm). After the incubation of lysosomal samples with pseudotyped SARS-CoV-2 virions at 37 °C for 1 h, the emission intensity of each lysosomal sample group from 700 nm to 850 nm was detected under the 673 nm excitation. The S2 protein was detected by WB with an anti-SARS-CoV-2 spike glycoprotein S2 antibody (Abcam, ab283913).

LysoTRAP degrading pseudotyped SARS-CoV-2 virions. 10 μg lysoTRAP was mixed with 5×10^8 TU SARS-CoV-2 pseudotyped virions at a rate of 1:5 (lysoTRAP: pseudotyped virion) and incubated at 37 °C (total volume: 1 mL). At the point-in-time of 0, 1, 4, 12, and 24 h, the compound was homogenized with RIPA and virion protein could be isolated according to the manufacturer's protocol (RIPA Lysis Buffer, P0013B, Beyotime). The protein levels of SARS-CoV-2 were determined by ELISA. Same procedures of above-mentioned ACE2 ELISA were applied. In brief, 96-well plates (Corning) were coated with above isolated protein, blocked in 5% bovine serum albumin, incubated with 100 μL of rabbit anti-P55 or anti-P24 and HRP-conjugated goat anti-rabbit secondary antibody pigmented with 3,3′,5,5′-tetramethylbenzidine, suspended with H_2SO_4 and measured the absorbance by a microplate reader.

To verify lysoTRAP degrading SARS-CoV-2 pseudotyped virus in the RNA levels, the compound of lysoTRAP and SARS-CoV-2 pseudotyped virions was homogenized with Trizol, and virus RNA could be isolated according to the RNAeasy™ Viral RNA Isolation Kit with Spin Column (R0035L, Beyotime). SARS-CoV-2 viral RNA levels were measured by commercially available BeyoFastTM SYBR Green One-Step qRT-PCR Kit (D7268s, Beyotime) on a CFX96 real-time PCR detection system (Bio-Rad) with *GFP* and *Luc* primers, respectively (sequences (Sangon Biotech): GFP-F, CATGTACCACGAGTCCAAGTTCTACG; GFP-R, CTCCCAGTTGTCGGTCATCTTCTTC; Luc-F, TACACCTTCGTGACT TCCCATTTGC; Luc-R, CAATCCGGTACTGCCACTACTGTTC). The PCR conditions were as follows: 50 °C for 15 min (reverse transcription), 95 °C for 2 min (predegeneration), 42 cycles of 95 °C for 15 s, and 60 °C for 30 s (amplification). The mRNA levels were normalized according to the result at 0 h.

To further verify the degradation capacity of lysoTRAP to SARS-CoV-2 pseudotyped virions, we used Bafilomycin A1 to inhibit acid accumulation in the lysosomes before isolating lysosomes from cells, obtaining neutralized lysosome. After incubation with SARS-CoV-2 pseudotyped virus, the levels of viral protein and viral RNA were detected by above mentioned method. Meanwhile, the inhibitor complex, including leupeptin (10 nM), Pepstatin A (10 nM), E-64 (10 nM), and RNase inhibitor (10 nM), was introduced into lysoTRAP by electroporation. After incubation with SARS-CoV-2 pseudotyped

virus, the levels of viral protein and viral RNA were detected by above mentioned method.

Pseudotyped virion infection assay. For the infection inhibition assay, ACE2-OE HEK-293T cells were seeded in 96-well plates (10,000 cells/well) and incubated at incubator for 1 d, and then treated with pseudotyped virus (5×10^4 TU/well) and lysoTRAP (100 µg/mL) at the same time for 2 d. In the assay, the molecular amount of ACE protein in the free ACE2 group is equal to the molecular amount of ACE protein presented on the lysoTRAP surface and the amount of lysosome in the naked lysosome group is equal to the amount of lysoTRAP. For microscopy imaging, the nuclei were stained DAPI and imaged by CLSM (A1/SIM/STORM, Nikon, Japan). For flow cytometry analysis, the cells were collected and analyzed by flow cytometry (Beckman coulter, CytoFLEX).

We also obtained serval pseudotyped SARS-CoV-2 variants, which were gifted from Professor Youchun Wang of Institute for Biological Product Control, National Institutes for Food and Drug Control (NIFDC), and WHO Collaborating Center for Standardization and Evaluation of Biologicals, Beijing, China. According to a reported method[47], these variants expressed a luciferase reporter gene and the virus infection were determined via the luminescence of each well, which was detected by multimode microplate reader (EnVision, PerkinElmer).

In vivo biodistribution of lysoTRAP

The biodistribution of lysoTRAP in mice. C57BL/6 mice were randomly divided into two groups (3 mice per group) and administrated with Cy7-labeled lysoTRAP (100 µg) via pulmonary inhalation and *i.v.* injection. At different time intervals, fluorescence imaging of mice was taken using an in vivo imaging system (FX Pro, 624 Kodak) with the Carestream MI software (v.5.0.7 version) with a 670 nm excitation wavelength and a 720 nm filter to collect the lysoTRAP signals. In the ex vivo imaging experiments, the mice were euthanized to extract organs following to capture again at 9 h post-administration. It should be noted that Cy7-SE was linked to the -NH2 of membrane proteins on lysoTRAP by a chemical bond. Considering the stable conjugation, it was reasonable to envision that Cy7-SE held a stable association on lysoTRAP in vivo and thus could adequately indicate lysoTRAP in tissues.

The inhalation treatment was conducted via liquid aerosol devices (Huironghe Company, Beijing, China), including a Micro Sprayer, small laryngoscope for mouse and nylon band, which was specifically design to fit the demand of mouse inhalation[49]. In brief, mice were anesthetized by the intraperitoneal injection of 500 mg/kg body weight avertin and then supported by a nylon band under its upper incisors and restrained on a slanted board (60 ° from the horizontal direction). The tracheal opening was visualized by inserting a laryngoscope; the Micro Sprayer, which is capable of ejecting liquid particles with a particle size of 5.02 ± 0.35 mm, was inserted 25 mm from the larynx (near the tracheal bifurcation) of the mouse. At each inhalation, 50 µl of lysoTRAP solutions or other was aerosolized into the lungs by depressing the Micro-Sprayer plunger with a constant force.

The biodistribution of lysoTRAP in lungs. To verify whether lysoTRAP uniformly distribute over the whole lung, light-sheet imaging was performed. C57BL/6 mice were administrated with Cy5-labeled lysoTRAP (100 µg) via pulmonary inhalation and then euthanized to extract lungs. Here, considering the commercialized light-sheet microscopy was equipped with the laser for the excitation of Cy5 rather than Cy7, we switched the dye from Cy7 to Cy5. The collected lungs were processed with Tissue-Clearing Reagent CUBIC (TCI) for tissue-clearing according to the manufacturer's instructions, which followed the fluorescence staining of lung trachea by streptavidin-FITC. In the end, the lungs were immersed in CUBIC-R+ reagent and

captured by light-sheet microscopy (Z.1, Zeiss, Germany). Image reconstructions were generated using Imaris v9.0 software.

The biodistribution of lysoTRAP in lung cells. C57BL/6 mice were administrated with Cy5-labeled lysoTRAP (100 µg) via pulmonary inhalation. The collected lungs fixed with 4% paraformaldehyde, dehydrated with 30% sucrose solution, embedded in OCT tissue compound and finally sectioned into 10 µm lung slides by freezing microtome (CM1950, Leica, Germany). To verify whether the ultimate destination of lysoTRAP were macrophages, the slides were stained with anti-F4/80 (rabbit), corresponding fluorescent secondary antibodies and DAPI, successively, and captured by CLSM (A1/SIM/STORM, Nikon, Japan).

Safety evolution of lysoTRAP. For comprehensive safety evaluations, the dosage, frequency, and source of lysoTRAP via pulmonary inhalation were included in the scope of investigation. For lung respiratory function, the respiratory frequency and tidal volume of mice were collected via FinePointe Whole-body Plethysmograph 4-Site System (WBP, BUXCO, American). For histological evaluation, dissected lungs and tracheas were sectioned into 10 µm slices and subsequently stained with hematoxylin and eosin (H&E), and then imaged by the Vectra platform (v 3.0.5, PerkinElmer, USA). For inflammatory cell recruitment, the proportion of macrophages (CD11b + F4/80 +), monocyte (CD11b + Ly6c + Ly6G-) and neutrophil (CD11b + Ly6c-Ly6G +) were measured using CytoFLEX LX flow cytometer (Beckman Coulter, USA), and analyzed using CytExpert software (version 2.3). For inflammatory factor release, the concentration of IL-6, TNF and IFN-γ in the lungs was detected by ELISA according to the manufacturer's instructions (Solarbio).

Mouse LAMP-1 and human ACE2 protein binding titers of serum IgG. C57BL/6 mice inhaled lysoTRAP at 0, 1, and 3 day. Serum of mouse was collected on 7, 14, 21, and 28 day. Binding titers of serum IgG to mouse LAMP-1 and human ACE2 protein were determined by ELISA. Briefly, 96-well plates (Corning) were coated with 1 µg/mL of mouse LAMP-1 or human ACE2 protein overnight at 4 °C in coating buffer, and blocked in 5% bovine serum albumin in PBS for 2 hours at 37 °C. Serially diluted serum was added to the ELISA plates and incubated for 1 hour at 37 °C. The plates were washed with 1× PBS containing 0.05% Tween-20 (PBST), followed by the addition of 100 µL of HRP-conjugated goat anti-mouse IgG with a 1:10000 dilution. After being incubated at 37 °C for 0.5 hours, plates were again washed with PBST. Then the plates were developed with 3,3',5,5'-tetramethylbenzidine for 10 min at room temperature, and the reaction was stopped with 2 M H$_2$SO$_4$. The absorbance at 450 nm was measured by a microplate reader. The endpoint titers were defined as the highest reciprocal dilution of serum to give an absorbance greater than 2.1-fold of the background values from control mice.

Programmed performance of lysoTRAP in capturing, internalizing, and degrading SARS-CoV-2 pseudotyped virions in vivo LysoTRAP capturing SARS-CoV-2 pseudotyped virions. 1×10^6 TU BODIPY-labeled pseudotyped virions were administrated into C57BL/6 mice via thoracic injection. 1 h later, the normal C57BL/6 mice were administered with Cy5-labeled lysoTRAP, naked lysosomes, or free ACE2 via pulmonary inhalation. At 1 d, mice were sacrificed, and lungs were collected and sectioned into 10 µm slices. After staining with DAPI, the lung slices were mounted for imaging by CLSM (A1/SIM/STORM, Nikon, Japan).

For thoracic injection, sterile hypodermic syringe matched with 28 G needle was inserted 4-7 mm from the side of the mouse's left chest between the 7th and 8th ribs. At each thoracic injection, 50 µl pseudotyped virions were injected into the pleural cavity by depressing the syringe with a constant force.

LysoTRAP degrading SARS-CoV-2 pseudotyped virions. 1×10^6 TU pseudotyped virions were administrated into C57BL/6 mice via thoracic injection. 1 h later, the normal C57 mice were administered with lysoTRAP, naked lysosomes, or free ACE2 via pulmonary inhalation. At 1 d or 2 d, mice were sacrificed and lungs were collected. Partial lungs were homogenized with RIPA to extract viral protein for subsequently WB analysis. Partial lungs were homogenized with Trizol to extract viral RNA for subsequently q-PCR analysis.

In vivo clearance of pseudotyped SARS-CoV-2 virions by lysoTRAP. Same pseudotyped virions inoculation and lysoTRAP inhalation procedures of above-mentioned normal C57BL/6 mice were applied in this model. In the ex-vivo imaging experiments, mice were sacrificed at 2 d and lungs were collected for imaging by using an IVIS imaging system (PerkinElmer, USA). For histological analysis, lungs were sectioned into 10 μm slices and stained with DAPI, which followed the imaging by CLSM (A1/SIM/STORM, Nikon, Japan).

In vivo clearance of authentic SARS-CoV-2 by lysoTRAP in hamster model. This study was conducted in a biosafety level 3 (BSL3) laboratory following institutional biosafety guidelines by the Institute of Medical Biology, Peking Union Medical College, Chinese Academy of Medical Sciences, Kunming, China. Briefly, hamsters were challenged with 2×10^4 50% tissue culture infective dose (TCID50) of authentic SARS-CoV-2 (CCPM-B-V-049-2112-18) via the intranasal route. Subsequently, the hamsters were randomized into two treatment groups, which received pulmonary inhalation of either PBS or lysoTRAP (prepared from lysosomes sourced from hamster macrophages) at a dose of 5 mg particles per kg of body weight at 1 h, 1 d and 2 d after challenge. At 3 d, the lung tissues were collected for viral burden and histological analysis.

For SARS-CoV-2 RNA copies detection, partial lungs were homogenized with Trizol, and isolated RNA were measured by q-PCR with commercially available One Step PrimeScript q-PCR Kit (RR064A, TCI) on a CFX96 real-time PCR detection system (Bio-Rad). The primers and probes published by WHO were used to detect RNA copies of SARS-CoV-2, with sequences (Sangon Biotech) as follows: E_Sarbeco-F, ACAGGTACGTTAATAGTTAATAGCGT; E_Sarbeco-R, ATATTGCAGCAGTACGCACACA; E_Sarbeco-probe, FAM-ACACTAGCCATCCTTACTGCGCTTCG-BHQ1; Omi-F, GACCCCAAAATCAGCGAAAT; Omi-R, TCTGGTTACTGCCAGTTGAATCTG; Omi-probe, FAM-ACTCCGCATTACGTTTGGTGGACC-BHQ1.

For histological analysis, lungs were sectioned into 10 μm slices and were successively stained with S fluorescent antibody and DAPI, and captured by CLSM (A1/SIM/STORM, Nikon, Japan). For pathological observation, the harvested left lungs were sectioned into 10 μm slices and subsequently stained with H&E, and then imaged by the Vectra platform. For inflammatory factor levels determination, partial lungs were homogenized with Trizol and processed with commercially available BeyoFastTM SYBR Green One-Step qRT-PCR Kit (D7268s, Beyotime) on a CFX96 real-time PCR detection system (Bio-Rad), with the primers sequences (Sangon Biotech) as follows: IL-6-F, AGGATACCACTCCCAACAGACCT; IL-6-R, CAAGTGCATCATCGTTGTTCATAC; TNF-F, GCCTCTTCTCATTCCTGCTT; THF-R, TGGGAACTTCTCATCCCTTTG; Actin-F, CACCATGTACCCAGGCATTG; Actin-R, CCTGCTTGCTGATCCACATC.

h-lysoTRAP trapping authentic SARS-CoV-2. This study was under institutional biosafety guidelines by the Sinovac Life Sciences Co., Ltd. All samples were heat-inactivated to eliminate any complement activity. For lysoTRAP capturing and internalizing authentic SARS-CoV-2 (SARS-CoV-2/human/CHN/CN1/2020, GenBank number MT407649.1), QCM assay and TEM (JSM-6700, JEOL, Japan) imaging were performed as described previously. For lysoTRAP degarding authentic SARS-CoV-2, proteomic and polypeptide analysis via LC-MS, and capillary

electrochromatography analysis and q-PCR detection were executed for determine the degradation of viral proteins and genome, respectively. For proteomic analysis, LC-MS was conducted by Q Exactive™ Hybrid Quadrupole-Orbitrap™ Mass Spectrometer with associated software (Thermo Proteome Discoverer, version 2.5.0.400) to analyze the degradation of SARS-CoV-2 proteins. Briefly, authentic SARS-CoV-2 virions were incubated with lysoTRAP. At the time points of 0 h, 2 h, 6 h, 12 h, and 24 h, sample materials were collected and analyzed with the same procedure as described for LC-MS based proteomic analysis of the lysosomes with or without LPS stimulation. The same amounts of tryptic peptides applied in LC-MS analysis ensured the normalization between each sample in the proteomics. For polypeptide analysis, degradation residue of SARS-CoV-2 proteins in the absence of trypsin digestion was filtered through a 10 kD strainer to isolated residual SARS-CoV-2 peptide, which was directly detected by LC-MS. Briefly, authentic SARS-CoV-2 virions were incubated with lysoTRAP or PBS solution. After 24 h incubation, PBS group was additionally added with same amount of lysoTRAP (anchored with disabled ACE2 protein) to match the protein concentration, and sample materials from PBS and lysoTRAP groups were collected. Then, the proteins of each sample were extracted by protein extraction solution containing 8 M urea and subsequently filtered through a 10 kD strainer to isolate residual SARS-CoV-2 peptides for analyzing degradation residue of SARS-CoV-2 proteins via polypeptide analysis. Finally, the obtained residual SARS-CoV-2 peptides were analyzed with the same procedure (step 3 to step 5; in the absence of step 1 and 2) as described for LC-MS based proteomic analysis of the lysosomes with or without LPS stimulation. The same amounts of residual peptides applied in LC-MS analysis ensured the normalization between each sample in the proteomics. For capillary electrochromatography analysis, capillary electrophoresis was conducted by QIAxcel Advanced (QIAGEN, Germany) with associated software (QIAxcel ScreenGel Software, version 1.6). For viral RNA levels determination, the isolated viral RNA was processed with commercially available BeyoFastTM SYBR Green One-Step qRT-PCR Kit (D7268s, Beyotime) on a CFX96 real-time PCR detection system (Bio-Rad), with the primers sequences (Sangon Biotech) as follows: ORF1a-F, GTTACTAAAATAAAACCTCATAATTCACATGAAG; ORF1a-R, AGTCCCTGTGAATTCATATATCTAAACT; ORF1b-F, ATGCTTACTAATGATAACACTTCAAGGTATTGGG; ORF1b-R, TTAATGTGACTCCATTAAGACTAGCTTGTTTGG; S-F, AACAATCTTGATTCTAAGGTTGGTG; S-R, GAAGTTCTTTTCTTGTGCAGG; ORF3a-F, AAAAGAGATGGCAACTAGCACTCTCC; ORF3a-R, GTAATACAACACAGTCTTTTACTCCAGATTCCC; E-F, GCTTTCGTGGTATTCTTGCTAGTTACAC; E-R, CACGAGAGTAAACGTAAAAAGAAGGTTTTACAAG; M-F, GCTTGCTGCTGTTTACAGAATAAATTGGA; M-R, AGAAAGCGTTCGTGATGTAGCAAC; ORF7a-F, CCTTGCTCTTCTGGAACATACGAGG; ORF7a-R, TCTTGAACTTCCTCTTGTCTGATGAACAG; ORF7b-F, TGCTTTTTAGCCTTTCTGCTATTCCTTG; ORF7b-R, TGCAGTTCAAGTGAGAACCAAAAGA; ORF8-F, TGATGACCCGTGTCCTATTCACTT; ORF8-R, TTAGGTTCCTGGCAATTAATTGTAAAAGGTAAACAG; N-F, CTACTACCGAAGAGCTACCAGACGA; N-R, CAGTTCCTTGTCTGATTAGTTCCTGGT; ORF10-F, TTACGATATATAGTCTACTCTTGTGCAG; ORF10-R, ACATCTACTTGTGCTATGTAGTTACG; Note that the copy area of each viral gene during q-PCR was in proportion to the length of each viral gene. The PCR conditions were as follows: 50 °C for 30 min (reverse transcription), 95 °C for 5 min (predegeneration), 42 cycles of 95 °C for 2 min, and 60 °C for 5 min (amplification). The mRNA levels were normalized according to the result at 0 h.

h-lysoTRAP clearing authentic SARS-CoV-2 on human lung organoids

Construction of human lung organoids. The human lung organoids were constructed by K2 ONCOLOGY company (China) according to a previously described method[50]. The surgery normal lung tissues adjacent to tumors were obtained from patients with advanced non-

small cell lung carcinoma after ethical approval were approved by the Biomedical Research Ethics Committee of Peking University First Hospital (No.2021-486) and informed consent from all participants or next of kin. The tissues were washed with cold phosphate-buffered saline (PBS) containing antibiotics and chopped into approximately 5 mm pieces with surgical scissors. Tissues were further washed with 10 mL advanced DMEM/F12 (Thermo Fisher Scientific, Waltham, MA) containing 1× Glutamax, 10 mM N-(2-hydroxyethyl)piperazine-N′-ethanesulfonic acid (HEPES), and antibiotics and digested in 10 mL advanced DMEM/F12 containing 2% fetal calf serum (FCS) and 2 mg/mL collagenase on an orbital shaker at 37 °C for 1–2 h. The pellet was resuspended in 10 mL advanced DMEM/F12 containing 2% FCS and centrifuged again at 400 g. Dissociated cells were collected in human organoid medium (OrganoProTM Huamn Lung Organoids Culture Kit, K2ONCOLOGY, China), suspended in growth factor reduced (GFR) Matrigel (Corning Inc., Corning, NY), and seeded. The Matrigel was then solidified and overlaid with 500 μL of complete human organoid medium, which was subsequently refreshed every 2 days.

h-lysoTRAP inhibiting authentic SARS-CoV-2 infection. This study was conducted in a biosafety level 3 (BSL3) laboratory following institutional biosafety guidelines by the Sinovac Life Sciences Co., Ltd. Cell clusters digested from human lung organoids were seeded in 96-well plates (1,000 cells/well) and incubated at incubator for 3-5 d. Then authentic SARS-CoV-2 (100 TCID50 /well) (SARS-CoV-2/human/CHN/CN1/2020, GenBank number MT407649.1 and SARS-CoV-2 Omicron variants) and h-lysoTRAP (100 μg/mL) were added into the 96-well plates and incubated at 37 °C in a 5% CO_2 incubator for 2 d. Here, EIDD-2801 and RBD antibody were singled out for reference and the amount of these two references matched the amount of ACE2 presented in the h-lysoTRAP. For SARS-CoV-2 RNA copies detection, lung organoids were homogenized with Trizol, and isolated RNA were measured by q-PCR with commercially available One Step PrimeScript q-PCR Kit (RR064A, TCI) on a CFX96 real-time PCR detection system (Bio-Rad). The primers and probes published by WHO were used to detect a region of E gene in the SARS-CoV-2 genome, with sequences (Sangon Biotech) as follows: E_Sarbeco-F, ACAGGTACGTTAATAGTTAA-TAGCGT; E_Sarbeco-R, ATATTGCAGCAGTACGCACACA; E_Sarbeco-probe, FAM-ACACTAGCCATCCTTACTGCGCTTCG-BHQ1 Omi-F, GACCCCAAAATCAGCGAAAT; Omi-R, TCTGGTTACTGCCAGTT-GAATCTG; Omi-probe, FAM-ACTCCGCATTACGTTTGGTGGACC-BHQ1. For immunofluorescent staining, lung organoids were successively stained with ACE2 fluorescent antibody, S1 fluorescent antibody and DAPI, and captured by CLSM (A1/SIM/STORM, Nikon, Japan). For cell apoptosis upon the lung organoids, supernatant per well was collected and processed with LDH Cytotoxicity Assay Kit (Beyotime) to detect the release of lactic dehydrogenase (LDH) from organoids.

lysoTRAP inhibiting influenza virus infection
Preparation and characterizations of lysoTRAP (SA). Distinct from the lysoTRAP clearing SARS-CoV-2, the baits of lysoTRAP clearing influenza virus (denoted as lysoTRAP (SA)) were Sialic Acids (SAs). Through a-2,6-sialyltransferases, an essential enzyme in the synthesis pathways of sialic acid oligosaccharides, SA could be decorated to the N-linked and O-linked glycosylation sites. Considering partial N-linked and O-linked glycosylation sites present on cytoplasmic tails of lysosomal membrane proteins, we could modify SA on the external surface of lysosomes, obtaining lysoTRAP (SA). Briefly, lysosomes purified according to above-mentioned method were mixed with cytidyl sialoside phosphate (CMP-Neu5Ac) and a-2,6-sialyltransferases at 37 °C. After 1 h incubation, the compound was processed with superhigh speed centrifugation to remove free CMP-Neu5Ac and a-2,6-sialyltransferases, and the precipitation was purified lysoTRAP (SA). To demonstrate the SA presented in the lysoTRAP (SA), the lysoTRAP (SA) was incubated with sambucus nigra lectin-AF488 and LAMP-2

fluorescent antibody in succession, followed by viewing by CLSM (A1/SIM/STORM, Nikon, Japan).

To explore the internalization mechanism of H1N1 by lysoTRAP (SA), FRET analysis was conducted. Briefly, lysosome or lysoTRAP lysosomal samples (naked lysosomes, lysoTRAP (SA) and lysoTRAP (SA) with Furin inhabator (1 nM chloromethylketone)) were labeled by Cy7-SE (excitation/emission: 755/785 nm), and pseudotyped SARS-CoV-2 virions were labeled by Cy5.5 (excitation/emission: 673/715 nm). After the incubation of lysosomal samples with pseudotyped SARS-CoV-2 virions at 37 °C for 1 h, the emission intensity of each lysosomal sample group from 700 nm to 850 nm was detected under the 673 nm excitation.

Preparation and characterizations of h-lysoTRAP (SA). The h-lysoTRAP (SA) was prepared from h-lysosome by mentioned SA described method. The degradation ability of h-lysoTRAP (SA) to H1N1-PR8 virus in vitro was tested by Western blotting, using the N protein of H1N1 antibody (Abcam, ab104870). The RNA copies of H1N1-PR8 virus were detected by q-PCR. To explore the clearance of h-lysoTRAP (SA) to H1N1 virus, the h-lysoTRAP (SA) and H1N1 virus were simultaneously added to lung organoid. After 24 h inoculation, the infection of lung organoid was detected by q-PCR and CLSM. After 24 h inoculation, the infection of lung organoid was detected by q-PCR and CLSM. To determine the contribution of SA binding, we mixed HA (hemagglutinin) with h-lysoTRAP (SA) for occupying the H1N1 viral binding domain, thus obtaining a h-lysoTRAP (SA) with a non-functional binding moiety (denoted as h-lysoTRAP (SA-HA)). Then, H1N1-PR8 virus and samples (PBS, h-lysoTRAP(SA-HA), or h-lysoTRAP) were added to human lung organoids, simultaneously. Viral infection was detected by CLSM imaging of N protein expression and q-PCR analysis of H1N1-PR8 RNA copies in human lung organoids.

The clearance of replicated virus by lysoTRAP (SA) and h-lysoTRAP (SA). Authentic H1N1-PR8 was mixed with MDCK cells or lung organoids, respectively. After 1 h of viral inoculation, H1N1-MDCK cells or H1N1-lung organoids mixture in the upper chamber of the TranswellTM model and untreated MDCK or lung organoids in the lower chamber, accompanied by the incubation of lysoTRAP (SA) or h-lysoTRAP (SA) in the upper chamber. After 3 days, the infection of MDCK cell or lung organoids in the lower chamber was detected by CLSM and q-PCR. N proteins (green) of H1N1 were stained with fluorescent antibody, the cytoskeleton (red) was stained by Nile red labeled phalloidin and the nuclei were stained with DPAI (blue).

LysoTRAP (SA) clearing influenza virus in mice model. This study was conducted in a BSL3 laboratory following institutional biosafety guidelines by the Academy of Military Medical Sciences. The PR8 strain and CA07 strain of influenza A virus (H1N1-PR8 and H1N1-CA07) were gifted from Professor Meng Qin of Beijing Advanced Innovation Center for Soft Matter Science and Engineering, College of Life Science and Technology, Beijing University of Chemical Technology, Beijing, China. About the trapping and clearing experiments in vitro were performed as above-mentioned in the SARS-CoV-2. C57BL/6 mice were challenged with 1000 TCID50 H1N1-PR8 or H1N1-CA07 via the intranasal route and lysoTRAP (SA) was administrated via pulmonary inhalation at 1 h and 2 d. At 5 d post-challenge, mice were euthanized and necropsied: mice and the lung were weighed and lung index was calculate as the weight of lung/the weight of mice; the harvested right lungs (about 0.1-gram lung) were homogenized with Trizol and processed with commercially available BeyoFastTM SYBR Green One-Step qRT-PCR Kit (D7268s, Beyotime) for viral RNA levels determination and inflammatory factor levels determination, with the primers sequences (Sangon Biotech) as follows: IL-6-F, AGGATACCAC TCCCAACAGACCT; IL-6-R, CAAGTGCATCATCGTTGTTCATAC; TNF-F, GCCTCTTCTCATTCCTGCTT; THF-R, TGGGAACTTCTCATCCCTTTG;

Actin-F, CACCATGTACCCAGGCATTG; Actin-R, CCTGCTTGCTGATC-CACATC; H1N1-PR8-R, GGTGACAGGATTGGTCTTGTCTTTA; H1N1-PR8-F, CTTCTAACCGAGGTCGAAACGTA; H1N1-CA07-R:AGGGCAT-TYTGGACAAAKCGTCTA; H1N1-CA07-F: GACCRATCCTGTCACCTCTG AC. The harvested left lungs were sectioned into 10 μm slices and subsequently stained with H&E, and then imaged by the Vectra platform for pathological examination.

Statistical analysis

To show inhibition profiles across treatment groups (EIDD-2801, RBD antibody and h-lysoTRAP) and analyze the discrepancy among infection indexes for wild-type and Omicron stain, principal component analysis (PCA), clustering analysis and the visualization were performed by relevant analysis tools in Omicsmart (https://www.omicshare.com/tools/Home/Soft/getsoft). For other data, GraphPad Prism 8.4.3 and Origin 2021b were utilized for plotting and statistical analysis. All data were presented as mean ± SD and significance were calculated by two-tailed unpaired Student's t-tests, or One-way ANOVA (ns, not significant; $*p < 0.05$; $**p < 0.01$; $***p < 0.001$; $****p < 0.0001$).

Reporting summary

Further information on research design is available in the Nature Portfolio Reporting Summary linked to this article.

Data availability

The main data supporting the results in this study are available within the paper and its Supplementary Information. Source data for main figures and Supplementary Figs. are available in Figshare (https://doi.org/10.6084/m9.figshare.27231987). The mass spectrometry and proteomics data are available from the ProteomeXchange Consortium (through the iProX partner repository) via the dataset identifier PXD056776, PXD056801, PXD056985 and PXD056987. Source data are provided with this paper.

References

1. Synowiec, A., Szczepanski, A., Barreto-Duran, E., Lie, L. K. & Pyrc, K. Severe Acute Respiratory Syndrome Coronavirus 2 (SARS-CoV-2): a Systemic Infection. *Clin. Microbiol. Rev.* **34**, 133–120 (2021).
2. Lamers, M. M. & Haagmans, B. L. SARS-CoV-2 Pathogenesis. *Nat. Rev. Microbiol.* **20**, 270–284 (2022).
3. Wiersinga, W. J., Rhodes, A., Cheng, A. C., Peacock, S. J. & Prescott, H. C. Pathophysiology, Transmission, Diagnosis, and Treatment of Coronavirus Disease 2019 (COVID-19): A Review. *JAMA* **324**, 782–793 (2020).
4. Hoffmann, M. et al. SARS-CoV-2 Cell Entry Depends on ACE2 and TMPRSS2 and Is Blocked by a Clinically Proven Protease Inhibitor. *Cell* **181**, 271–280.e278 (2020).
5. Zhang, H. et al. APOE Interacts with ACE2 Inhibiting SARS-CoV-2 Cellular Entry and Inflammation in COVID-19 Patients. *Signal. Transduct. Target. Ther.* **7**, 261 (2022).
6. Wang, Q. et al. Structural and Functional Basis of SARS-CoV-2 Entry by Using Human ACE2. *Cell* **181**, 894–904.e899 (2020).
7. Tao, K. et al. SARS-CoV-2 Antiviral Therapy. *Clin. Microbiol. Rev.* **34**, e0010921 (2021).
8. Muecksch, F. et al. Affinity Maturation of SARS-CoV-2 Neutralizing Antibodies Confers Potency, Breadth, and Resilience to Viral Escape Mutations. *Immunity* **54**, 1853–1868 e1857 (2021).
9. Xia, S. et al. Inhibition of SARS-CoV-2 (previously 2019-nCoV) Infection by a Highly Potent Pan-coronavirus Fusion Inhibitor Targeting its Spike Protein that Harbors a High Capacity to Mediate Membrane Fusion. *Cell Res.* **30**, 343–355 (2020).
10. Yang, C. et al. Salvianolic Acid C Potently Inhibits SARS-CoV-2 Infection by Blocking the Formation of Six-helix Bundle Core of Spike Protein. *Signal. Transduct. Target. Ther.* **5**, 220 (2020).
11. Weissman, D. et al. D614G Spike Mutation Increases SARS CoV-2 Susceptibility to Neutralization. *Cell Host Microbe* **29**, 23–31.e24 (2021).
12. Harvey, W. T. et al. SARS-CoV-2 Variants, Spike Mutations and Immune Escape. *Nat. Rev. Microbiol.* **19**, 409–424 (2021).
13. Wang, Z. et al. mRNA Vaccine-elicited Antibodies to SARS-CoV-2 and Circulating Variants. *Nature* **592**, 616–622 (2021).
14. Collier, D. A. et al. Sensitivity of SARS-CoV-2 B.1.1.7 to mRNA Vaccine-Elicited Antibodies. *Nature* **593**, 136–141 (2021).
15. Tao, K. et al. The Biological and Clinical Significance of Emerging SARS-CoV-2 Variants. *Nat. Rev. Genet.* **22**, 757–773 (2021).
16. Liu, L. et al. Striking Antibody Evasion Manifested by the Omicron Variant of SARS-CoV-2. *Nature* **602**, 676–681 (2022).
17. Cornish, E. F., Filipovic, I., Asenius, F., Williams, D. J. & McDonnell, T. Innate Immune Responses to Acute Viral Infection During Pregnancy. *Front. Immunol.* **11**, 572567 (2020).
18. Bryden, S. R. et al. Pan-viral Protection against Arboviruses by Activating Skin Macrophages at the Inoculation Site. *Sci. Transl. Med.* **12**, eaax2421 (2020).
19. Merad, M. & Martin, J. C. Pathological Inflammation in Patients with COVID-19: a Key Role for Monocytes and Macrophages. *Nat. Rev. Immunol.* **20**, 355–362 (2020).
20. Hoepel, W. et al. High Titers and Low Fucosylation of Early Human Anti-SARS-CoV-2 IgG Promote Inflammation by Alveolar Macrophages. *Sci. Transl. Med.* **13**, eabf8654 (2021).
21. Wang, Z., Li, S. & Huang, B. Alveolar Macrophages: Achilles' heel of SARS-CoV-2 Infection. *Signal. Transduct. Target. Ther.* **7**, 242 (2022).
22. Lian, Q. et al. Differential Effects of Macrophage Subtypes on SARS-CoV-2 Infection in a Human Pluripotent Stem Cell-derived Model. *Nat. Commun.* **13**, 2028 (2022).
23. Kalyoncu, E., Ahan, R. E., Ozcelik, C. E. & Seker, U. O. S. Genetic Logic Gates Enable Patterning of Amyloid Nanofibers. *Adv. Mater.* **31**, e1902888 (2019).
24. Shen, W., Zhong, H., Neff, D. & Norton, M. L. NTA Directed Protein Nanopatterning on DNA Origami Nanoconstructs. *J. Am. Chem. Soc.* **131**, 6660–6661 (2009).
25. Rawlings, N. D. & Barrett, A. J. MEROPS: the peptidase database. *Nucleic Acids Res.* **38**, 227–233 (2010).
26. Trivedi, P. C., Bartlett, J. J. & Pulinilkunnil, T. Lysosomal biology and function: modern view of cellular debris bin. *Cells* **9**, 1131 (2020).
27. Kreye, J. et al. A Therapeutic Non-self-reactive SARS-CoV-2 Antibody Protects from Lung Pathology in a COVID-19 Hamster Model. *Cell* **183**, 1058–1069 (2020).
28. Imai, M. et al. Syrian Hamsters as a Small Animal Model for SARS-CoV-2 Infection and Countermeasure Development. *Proc. Natl Acad. Sci. USA* **117**, 16587–16595 (2020).
29. Salahudeen, A. A. et al. Progenitor Identification and SARS-CoV-2 Infection in Human Distal Lung Organoids. *Nature* **588**, 670–675 (2020).
30. Katsura, H. et al. Human Lung Stem Cell-Based Alveolospheres Provide Insights into SARS-CoV-2-Mediated Interferon Responses and Pneumocyte Dysfunction. *Cell Stem Cell* **27**, 890–904.e898 (2020).
31. Han, Y. et al. Identification of SARS-CoV-2 Inhibitors using Lung and Colonic Organoids. *Nature* **589**, 270–275 (2021).
32. Schultz, D. C. et al. Pyrimidine Inhibitors Synergize with Nucleoside Analogues to Block SARS-CoV-2. *Nature* **604**, 134–140 (2022).
33. Wec, A. Z. et al. Broad Neutralization of SARS-related Viruses by Human Monoclonal Antibodies. *Science* **369**, 731–736 (2020).
34. Long, J. S., Mistry, B., Haslam, S. M. & Barclay, W. S. Host and viral determinants of influenza A virus species specificity. *Nat. Rev. Microbiol.* **17**, 67–81 (2019).
35. Yamada, S. et al. Haemagglutinin mutations responsible for the binding of H5N1 influenza A viruses to human-type receptors. *Nature* **444**, 378–382 (2006).

36. Li, Z. et al. Cell-mimicking Nanodecoys Neutralize SARS-CoV-2 and Mitigate Lung Injury in a Non-human Primate Model of COVID-19. *Nat. Nanotechnol.* **16**, 942–951 (2021).

37. Zhang, H. et al. Inhalable Nanocatchers for SARS-CoV-2 Inhibition. *Proc. Natl. Acad. Sci. USA* **118**, e2102957118 (2021).

38. Xie, F. et al. Engineering Extracellular Vesicles Enriched with Palmitoylated ACE2 as COVID-19 Therapy. *Adv. Mater.* **33**, e2103471 (2021).

39. Zhang, Q. et al. Cellular Nanosponges Inhibit SARS-CoV-2 Infectivity. *Nano Lett.* **20**, 5570–5574 (2020).

40. Hoffmann, M. et al. SARS-CoV-2 Variants B.1.351 and P.1 Escape from Neutralizing Antibodies. *Cell* **184**, 2384–2393 (2021).

41. Krause, P. R. et al. SARS-CoV-2 Variants and Vaccines. *N. Engl. J. Med.* **385**, 179–186 (2021).

42. Bonifacino, J. S. & Traub, L. M. Signals for sorting of transmembrane proteins to endosomes and lysosomes. *Annu. Rev. Biochem.* **72**, 395–447 (2003).

43. Ender, P. v. Intracellular Recycling and Cross-presentation by MHC class I Molecules. *Immunol. Rev.* **272**, 80–96 (2016).

44. Dendrou, C. A., Petersen, J. & Rossjohn, J. L. HLA variation and disease. *Nat. Rev. Immunol.* **18**, 325–339 (2018).

45. Dominique, C. et al. Human plasma Thioredoxin-80 increases with age and in apoE–/– mice induces inflammation, angiogenesis and atherosclerosis. *Circulation* **136**, 464–475 (2017).

46. Wang, S. et al. Macrophage-tumor chimeric exosomes exert spatiotemporally synergistic anticancer effects through dual-targeting to lymph nodes and tumor. *Sci. Transl. Med.* **13**, eabb6981 (2021).

47. Nie, J. et al. Quantification of SARS-CoV-2 neutralizing antibody by a pseudotyped virus-based assay. *Nat. Protoc.* **15**, 3699–3715 (2020).

48. Gong, C. et al. Tumor Exosomes Reprogrammed by Low pH Are Efficient Targeting Vehicles for Smart Drug Delivery and Personalized Therapy against their Homologous Tumor. *Adv. Sci.* **8**, 2002787 (2021).

49. Feng, J. et al. Enhanced protection against Q fever in BALB/c mice elicited by immunization of chloroform-methanol residue of Coxiella burnetii via intratracheal inoculation. *Vaccine* **37**, 6076–6084 (2019).

50. Xie, J. et al. An artemisinin derivative ART1 induces ferroptosis by targeting the HSD17B4 protein essential for lipid metabolism and directly inducing lipid peroxidation. *CCS Chem.* **4**, 304–317 (2022).

Acknowledgements

Author contributions

W. W. and G. M. conceived, designed, and supervised the study. C. L., and X. H. performed the main experiments. Y. W., and W. H. provided serval pseudotyped virions and guided pseudotyped virion infection assay. Z. H., and M. Q. provided constructive suggestions and opinions on viral challenge experiments. Z. H., Y. L., and F. Y. performed the main experiments of authentic SARS-CoV-2 challenge on hamster model. X. L., Y. C., and X. P. contributed to the construction of human lung organoids and h-lysoTRAP. Y. Z., E. W., and Y. H. contributed to the evaluations of h-lysoTRAP trapping authentic SARS-CoV-2 and clearing authentic SARS-CoV-2 in organoids. M. Q. guided the trapping experiments of lysoTRAP and provided the influenza A virus. L. Z. contributed to the proteomic analysis of SARS-CoV-2. L. Z., and D. W. contributed to the influenza A virus challenge on mouse model. Z. J., G. L., S. W., and X. Z. contributed to the evaluations of pulmonary delivery and the in vivo evolutions of clearing pseudotyped SARS-CoV-2. H. K. guided the construction and characterizations of lysoTRAP. C. L., X. Z., S. W., and H. K. aided in data analysis. C. L., and W. W. wrote the manuscript. W. W. and G. M. revised the manuscript. All authors discussed the results and commented on the manuscript.

Competing interests

The authors declare no competing interests.

Additional information

Supplementary information The online version contains supplementary material available at https://doi.org/10.1038/s41467-024-54505-6.

Correspondence and requests for materials should be addressed to Guanghui Ma or Wei Wei.

Peer review information *Nature Communications* thanks the anonymous reviewer(s) for their contribution to the peer review of this work. A peer review file is available.

Reprints and permissions information is available at http://www.nature.com/reprints

Publisher's note Springer Nature remains neutral with regard to jurisdictional claims in published maps and institutional affiliations.